DYNAMIC MODELING OF BELT DRIVES USING THE ELASTIC/PERFECTLY-PLASTIC FRICTION LAW

A Thesis
Presented to
The Academic Faculty

by

Dooroo Kim

In Partial Fulfillment
of the Requirements for the Degree
Master of Science in the
Department of Mechanical Engineering

Georgia Institute of Technology
August 2009

DYNAMIC MODELING OF BELT DRIVES USING THE ELASTIC/PERFECTLY-PLASTIC FRICTION LAW

Approved by:

Michael Leamy, Committee Chair
Department of Mechanical Engineering
Georgia Institute of Technology

Aldo Ferri
Department of Mechanical Engineering
Georgia Institute of Technology

Dr. Mark Costello
Department of Aerospace Engineering
Georgia Institute of Technology

Date Approved: 26 June 2009

ACKNOWLEDGEMENTS

I would like to thank my family for believing in me and supporting me throughout my career at Georgia Tech. I would also like to thank my advisor, Dr. Michael Leamy, and my co-advisor, Dr. Aldo Ferri, for their support and guidance while working on my thesis. I would like to thank my previous advisor, Dr. William Singhose, for preparing me for graduate school and teaching me some valuable lessons in research. I would also like to thank the graduate and undergraduate students that have made my time at Georgia Tech a great experience.

TABLE OF CONTENTS

LIST OF TABLES

LIST OF FIGURES

SUMMARY

Belt drives are used in numerous applications to transmit power between various machine elements. Some common applications include transportation vehicles, household appliances such as vacuum cleaners and washing machines, and devices driven by electric motors such as power machine tools. Belt drives come in various types, such as: flat belts, serpentine belt drives, v-belt drives and push belts for continuously variable transmissions (CVT). One limitation of the use of belt drives is the poor convergence of complex models that predict their operating conditions. This draw back greatly restricts the application of belt drive systems in other important manufacturing industries. A source of convergence failure is the sharp discontinuities in the solution due to the Coulomb friction model. It is believed that the inclusion of an elastic/perfectly-plastic friction law into the belt/pulley contact mechanics can yield mathematical models with enhanced accuracy and convergence. This friction model more accurately captures the true behavior of an elastic belt that exhibits microslip prior to fully-developed slip than previous regularized friction models. However, before this EPP friction model is applied to v-belts, the behavior of the EPP friction model is first investigated on a simpler, flat belt system. This allows us to compare our new model to previously developed friction laws.

The Elastic/Perfectly-Plastic friction model was introduced and applied to a two-pulley flat belt system. The equations of motions and the equilibrium solutions were derived using Hamilton's Principle. Solution to these equations is difficult because of the piece-wise linear nature of the governing partial differential equations. The stability of the perturbations to the steady-solutions was determined from an eigenvalue/eigenvector analysis, and it was found that the steady-state solution was stable. The results with analytical solution developed in this thesis matched very well with the results from a finite element model. It was found that the EPP model had no slope discontinuities in the normal force. However, the results with Coulomb's Law did produce slope discontinuities in the normal force. The

elimination of these slope discontinuities could potentially help alleviate convergence issues for more complex models. It was also found that if the EPP spring stiffness is too small, then the belt cannot undergo the prescribed tension change. If the value for the EPP spring stiffness is too large, then the EPP model approaches Coulomb's Law and sharp changes appear at the transition angle. Therefore, the EPP spring stiffness must be chosen appropriately such that the belt can still undergo the prescribed tension change, but also not too large that sharp changes in slope appear at the transition point.

The Elastic/Perfectly-Plastic friction model was applied to a previously developed v-belt model. It was found that the solutions to the governing equations with the EPP friction model was similar to the solutions with the Coulomb friction model. The convergence properties of the v-belt model with EPP friction was also very similar to that with Coulomb friction. When compared to the model with Coulomb friction, the range of possible high tensions for a given low tension was reduced slightly by 0.2% for the EPP friction. Convergence fails due to sharp changes of the inclination angle and the sliding angle on both pulleys for low and high tension spans. Because the sharp changes occur when the belt exits the pulley, the belt is in the fully-slipping zone and the EPP friction model cannot smooth the slope discontinuities.

CHAPTER I

INTRODUCTION

Belt drives are used in numerous applications to transmit power between various machine elements. Some common applications include transportation vehicles, household appliances such as vacuum cleaners and washing machines, and devices driven by electric motors such as power machine tools. Belt drives come in various types, such as: flat belts, serpentine belt drives, v-belt drives and push belts for continuously variable transmissions (CVT). The two types of belts discussed in this thesis are the traditional flat belt and the rubber v-belts, shown in Figures 1(a) and 1(b), respectively. These belts transmit power between two pulleys, as shown in Figure 2.

Flat belts are typically used in high-speed applications, while the v-belt is more appropriate for high-torque applications. Flat belts are simple, but tend to slip on the pulley face when heavy loads are applied. The v-belt is preferred for high-torque applications because the v-belt tends to wedge into the pulley groove as tension increases. The v-belt can be used in two different types of pulley systems. The first is a fixed pulley system with a mating groove, as shown in Figure 3(a). In these cases, the pulleys do not translate. The second is a system where the pulleys can translate and each consists of two mating, conical sides.

A common application of this second v-belt system is the continuously variable transmission (CVT) system, shown in Figure 3(b). The movable conical pulleys halves can create a continuous variation in the gear ratio. The control systems of v-belt drives for CVT's can control slip by compressing the two conical pulleys together. However, this action decreases the efficiency of the belt drive. Therefore, to enable efficient control of slip, it is vital that slip be accurately predicted. Because of the complexity of the numerous variables that govern the motion of the v-belt, reliable convergence of v-belt models can be difficult to achieve.

The main goal of this work is to improve the convergence of numerical simulations of

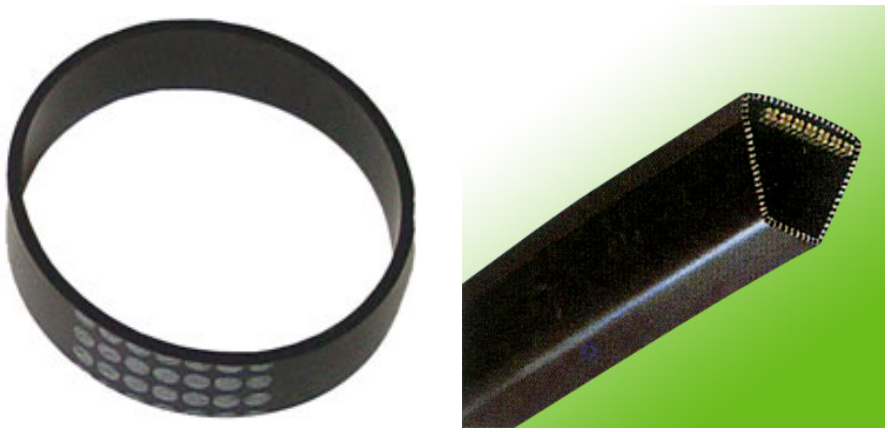

(a) Flat Belt. (b) V-Belt.

Figure 1: Pictures of a Flat Belt and a V-Belt [27, 26].

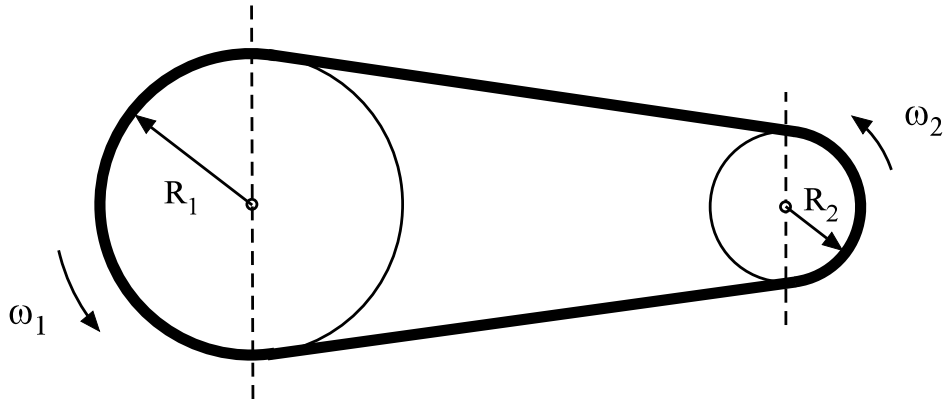

Figure 2: Two Pulley Flat Belt System.

complex systems such as v-belts in continuously variable transmissions. Current models have very poor convergence and are not suitable for manufacturing use in industry. An improved v-belt model can make CVT's more commercially feasible for car manufacturers, decrease the cost of hybrid cars for the consumer, and reduce carbon emission of vehicles. Once the behavior of the CVT are modeled, it will assist designers in rapidly determining the following:

1. the required setup tension to avoid slip during steady-state operation,
2. the maximum steady-state torque rating for a given design,
3. the shifting behavior of the CVT under load,

(a) V-Belt Pulley with Fixed Sheeves.

(b) V-Belt with Variable Pulleys for CVT's.

Figure 3: Pictures of Pulleys for V-Belts [28, 25].

4. the friction and creep profile to gross slip under steady-state and transient shifting,
5. the efficiency of the drive during steady-state operation, and
6. the variator parameters required to minimize slip, minimize sufficient contact pressure, and increase efficiency.

Then, the v-belt models can be incorporated into CVT models to create a control method for better CVT operation. Ultimately, the use of this model can be used to develop a control method to improve the efficiency of hybrid vehicles. This control-based model will enable a US automotive company to develop, test, and improve their CVT design while being cost effective for the consumer. An improved model has the potential to help clear obstacles impeding progress in hybrid vehicles production and ultimately, reduce the cost of hybrid

vehicles, making them more affordable to the average consumer and more widely used.

In this thesis, the Elastic/Perfectly-Plastic friction law will also be applied to v-belts. Gerbert and Sorge [6] developed a third-order model to predict the sliding of a v-belt in grooves. They also modeled the radial friction from seating and unseating of the belt. Seating occurs when a v-belt wedges into the groove of a pulley. Gerbert and Sorge determined there was an adhesive-like contact between the belt and pulley interface where the belt does not stick to the pulley but passes through a region where sliding occurs at an extremely small relative velocity. They developed the governing equations for steady motion for the driver or driven pulleys individually. The equations were solved using a shooting technique where the boundary value problem was converted to an initial value problem. However, Gerbert and Sorge's model required very accurate initial conditions to achieve convergence.

Kong and Parker [12] improved on Gerbert and Sorge's model by extending the model to a coupled two-pulley system with equal pulley radii. Belt inertia was included in the formulation. Kong and Parker were able to achieve better convergence by solving the boundary value problem for the entire drive for a specified tension span. They were able to find solutions for a wider range of parameters than Gerbert and Sorge. However, they did find tension ranges where the model could not find a solution. The difficulties were attributed due to sharp changes in slope for some belt states in the belt-pulley contact zones.

Previous studies in v-belt drives only utilized Coulomb friction and each had convergence difficulties. This thesis seeks to reduce these difficulties by applying the Elastic/Perfectly-Plastic friction model to v-belt drives. The EPP friction model is used instead of previous regularized friction models, such as the Creep-Rate-Dependent friction model, because the EPP model more accurately captures the true behavior of an elastic belt that exhibits microslip prior to fully-developed slip. The v-belt model presented in this thesis was modified from [12] to support the EPP friction model, and will be compared to Kong and Parker's v-belt model with Coulomb's Law. This analysis, the belt tension, belt radial displacement, belt inclination angle, and the belt axial displacement are considered. Except for belt axial displacement, the procedure to solve for these solutions are the same as in their paper and

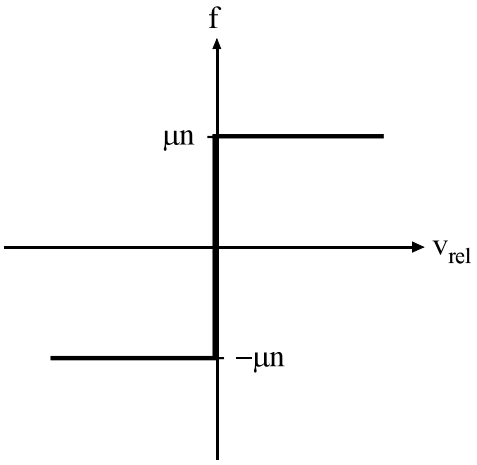

Figure 4: Coulomb Friction Law.

additional information on specific solving procedures can be found in [12].

In this thesis, a nontraditional friction model is employed termed the Elastic/Perfectly-Plastic (EPP) friction model. This new friction model has the potential improve convergence properties of complex belt drive systems, such as the v-belt for CVT's. However, before this EPP friction model is applied to v-belts, the behavior of the EPP friction model is first investigated on a simpler, flat belt system. This allows us to compare our new model to previously developed friction laws.

1.1 Friction on Flat Belt Drives

The friction interaction between belts and pulleys is very important in the study of belt mechanics. The effects of friction on flat belt drives have been investigated by numerous researchers and thorough reviews have been published [5, 3].

1.1.1 Coulomb Friction

Of the various friction models explored, the most frequently used model is Coulomb's Law. The relationship between the friction force, f, and the relative velocity of the two surfaces, v_{rel}, is depicted in Figure 4. The Coulomb friction law assumes that the bodies in contact are rigid and the frictional force is equal to the coefficient of friction, μ, times the normal force, n. The Coulomb friction law, as used in traditional classical creep analysis, only

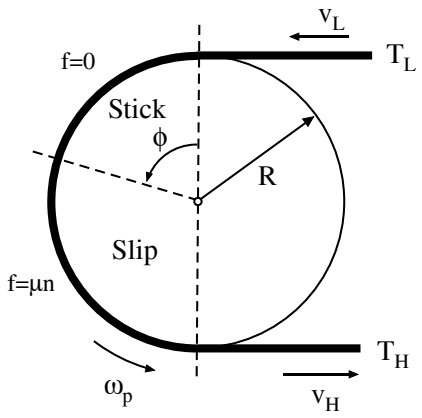

Figure 5: Adhesion and Slip Zones on Pulley with Coulomb Friction.

depends on the sign of the relative motion between the belt and the pulley surfaces. The classic creep theory is reviewed by Johnson [8], while more recently, Bechtel et al. [1] extended this theory to include inertial effects. Rubin [23] derived a closed-form solution for the mechanics of an extensible belt.

When the belt and pulley are at steady state velocity, the Coulomb friction law can produce one adhesion zone and one slip zone on the pulley surface. The adhesion zone begins at the point of contact with the pulley and ends at the beginning of the slip zone. The slip zone then continues along the belt/pulley interface until the belt leaves the pulley. These two zones are shown in Figure 5. In the slip zone, the friction force is fully developed and acts in the opposite direction of the pulley rotation. Historically, Coulomb's Law has been used in models because of its simplicity. However, it also creates discontinuities in the tension and friction force slopes [9] that can produce difficulties during numerical simulation.

1.1.2 Creep-Rate-Dependent Friction

The numerical difficulties posed by the discontinuity in Coulomb's Law has motivated the use of "smooth" or "regularized" approximate models. One such friction model is the Creep-Rate-Dependent friction model [21, 17]. The relationship between the friction force and relative velocity for this model is depicted in Figure 6. The Creep-Rate-Dependent friction model depends on both the direction and magnitude of the relative velocity between the belt and pulley, v_{rel}. A closed-form solution to the tri-linear frictional creep-rate law on belt

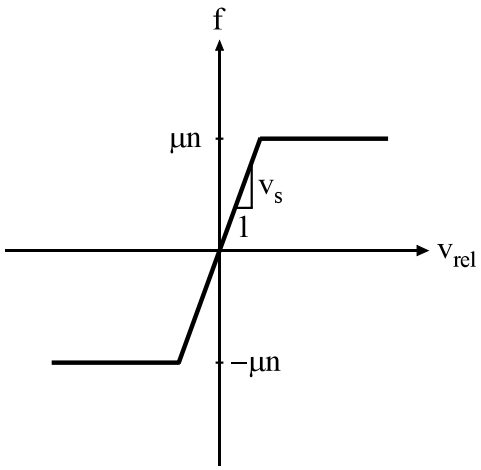

Figure 6: Creep-Rate-Dependent Friction Model.

drives was developed by Leamy and Wasfy [14, 15]. Although the Creep-Rate-Dependent friction model alleviates numerical difficulties, its drawback is that it does not correlate easily with friction phenomenon at the microscopic level.

Unlike the Coulomb friction law, the Creep-Rate-Dependent friction law cannot have an adhesion zone along the pulley [15]. This is because if an adhesion zone did exist, the belt would move with the same velocity as the rigid pulley, maintain a constant strain, and experience no friction forces. Because no torque is transmitted, this would violate Newton's second law of motion. Therefore, only solutions with no adhesion zones are valid. The pulley/belt interface can have a single sliding zone, where the friction force increases along the pulley surface, or two sliding zones, where the second zone has a constant friction force. These two zones depend on the friction slope parameter, v_s, and the relative velocity.

1.1.3 Elastic/Perfectly-Plastic and Microslip Friction

Because Coulomb's Law does not account for deformation prior to slipping, friction models better suited for elastic bodies are needed. In this thesis, friction is modeled as an elastic spring, with spring constant, k_f, in series with an ideal Coulomb damper, as shown in Figure 7. In elastic-plastic deformation studies, this friction model is referred to as the Elastic/Perfectly-Plastic (EPP) friction model [4].

Menq, et al. [20] modified this EPP law to accommodate microslip for simple, flexible

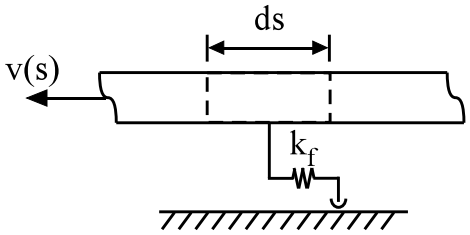

Figure 7: EPP Friction Modeled as a Spring and Damper.

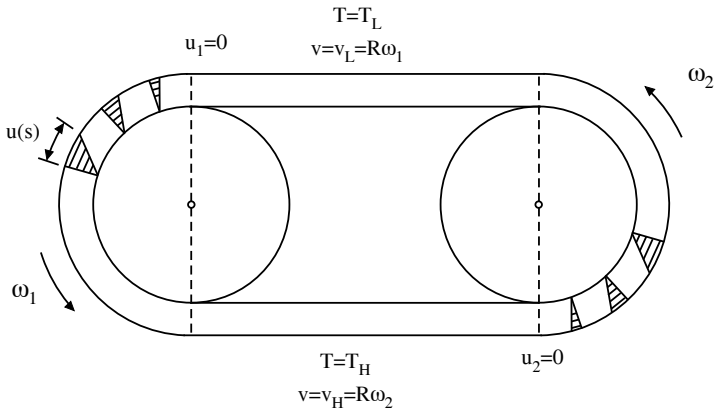

Figure 8: Shear in Belt Drive.

beams. The microslip model describes a beam interface where one section is sliding while the other section is stuck. Kong and Parker [9] extended this microslip friction model to the application of belt drives and included shear effects. Their model was applied to a two-pulley drive with equal pulley radii and an iteration method was proposed to find the steady-state mechanics. Belt inertia, which was previously neglected, was also included to improve modeling accuracy.

In the Kong and Parker model, the belt can either stick to or slide along the pulley surface. It is assumed that friction forces exist in the adhesion zones. In creep theory, no friction forces exist in the adhesion zone and no moment can be transmitted. However, in the microslip model, moment can be transmitted in the adhesion zone, and it is possible that only an adhesion zone exists (no sliding) due to static friction forces.

A typical elastic belt consists of strong tension-bearing cords surrounded by an elastic material, as shown in Figure 9. The bottom of the belt is in contact with the pulley surface.

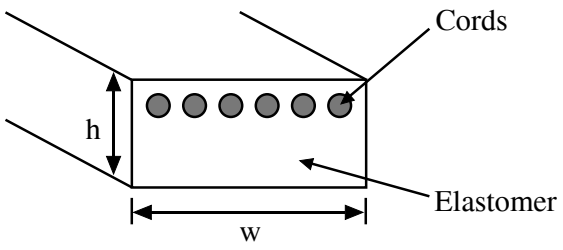

Figure 9: Cross-Section of a Flat Belt.

In the Kong and Parker model, the belt has a low width-to-height ($\frac{w}{h}$) ratio. Therefore, the friction forces develop in the elastic section of the belt, as shown in Figure 8. Their model also assumes that the belt cord and pulley speeds are unequal at the pulley entry points. But at belt entry points, it is assumed that the belt lower surface sticks to the pulley surfaces, and the axial displacement is zero. The axial displacement of the tension-bearing member relative to the pulley comes from two components: i) the speed difference between the belt and the pulley and ii) longitudinal stretching of the belt.

It is assumed in this study that the belt is stiff in shear and has a large width-to-height ratio. Therefore, even though the belt and friction model is similar to the microslip model in [9], the load-bearing tension cords experience no appreciable velocity difference compared to the belt surface in contact with the pulley. As a result, the tension difference is not due to the relative velocity between the belt and pulley, but rather to the inlet and outlet tension difference.

Kong and Parker discovered that with their microslip model, there are friction force slope discontinuities at the transition points between zones, but the slopes are smooth in the tension distribution. In the creep model, slope discontinuities exist for both the friction and tension distributions. However, the method presented in Kong and Parker requires an iteration process to find a solution.

1.2 Axially-Moving Continua

The flat belt drive considered in this thesis is modeled as an axially-moving rod, as shown in Figure 10. Axially-moving continua have received much attention in the application

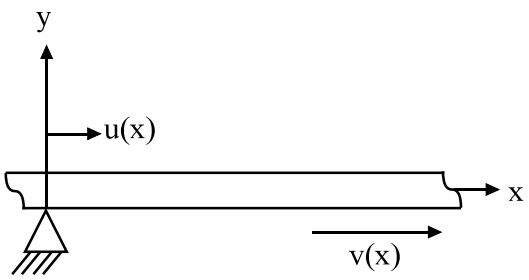

Figure 10: Axially Moving Beam.

of belt drives, and a review of such axially-moving structures is given in [30, 22]. Axially-moving continua are inherently gyroscopic, and vibration analysis of such systems have been conducted using a variety of methods, including Galerkin's method [22, 7], finite element methods, and modal analysis [31, 29].

Wickert developed a modal analysis procedure for both axially-moving strings and beams [31, 29]. He showed that a divergence instability occurs for a certain critical transport speed and that the importance of the nonlinear terms increases with transport speed. Lee and Jang [16] further investigated axially-moving finite and semi-infinite beams with four different boundary conditions. They found that for finite beams, the undamped responses are periodic and the fundamental frequency decreases with increasing axial speed. For infinite beams, the fundamental frequency also decreases with increasing speed but the responses are damped out with time. [11]

In this thesis, the belt band is modeled as a moving rod with no bending stiffness subject to specified boundary conditions. The rod boundary conditions are specified as simply-supported and free. At steady state, the linearized beam motion is utilized. Wickert and Mote derived the nonlinear equations of motion for transverse vibration of an axially moving material [30]. Beikmann, et al. later extended this model to the application of serpentine belts [2]. A picture of a serpentine belt drive is shown in Figure 11. Transverse displacement has been studied more than axial displacement, as in vibration of serpentine belt drives, because the transverse displacement is usually much larger than axial displacement.

The contributions of this thesis are to:

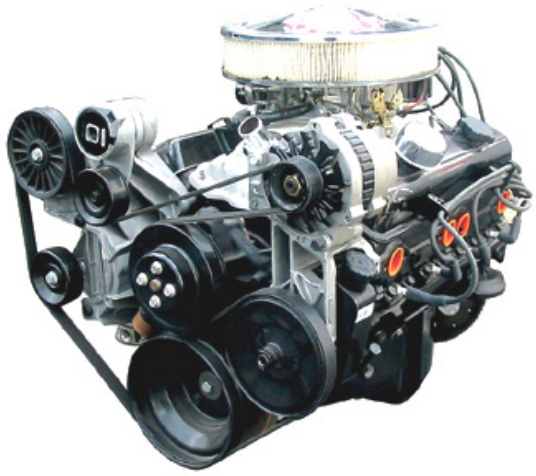

Figure 11: Serpentine Belt Drive.

1. employ a nontraditional friction model called the Elastic/Perfectly-Plastic friction model.

2. investigate the stability of the nonlinear system as a result of this new Elastic/Perfectly-Plastic friction model.

3. evaluate this friction model by comparing its prediction to Coulomb's Law and a finite element model.

4. extend the Elastic/Perfectly-Plastic friction model to the application of v-belt drives.

5. evaluate the EPP friction model for v-belts and compare to results with Coulomb's Law

In the next chapter, the Elastic/Perfectly-Plastic (EPP) friction model is presented. It is compared to previous friction models, and applied to a flat belt drive system with pulleys of equal radii. Hamilton's Principle is used to derive the nonlinear equations of motion which are then linearized about a steady-state configuration. The resulting equilibrium solutions are investigated and a minimum value for the EPP spring constant is found in closed-form. A stability analysis demonstrates that the nonlinear equilibrium solution is stable under

local perturbation. Results are compared to results generated by a dynamic finite element model. Chapter 3 discusses the EPP friction model extended to the v-belt model and the results are compared to results with Coulomb's Law. Finally, the conclusions of this thesis are discussed in Chapter 4.

CHAPTER II

THE EPP FRICTION LAW FOR FLAT BELT ANALYSIS

2.1 The Elastic/Perfectly-Plastic Friction Model

The Elastic/Perfectly-Plastic (EPP) friction model is employed in this study to provide a more accurate description of the true behavior of an elastic belt that exhibits microslip prior to fully-developed slip. The inclusion of elastic contact deformation is expected to help alleviate high parameter sensitivities encountered in previous belt drive studies. This may be particularly beneficial in the study of complex systems, such as v-belts for continuously variable transmissions. Previous v-belt studies used only the Coulomb friction law and required very accurate parameter values to achieve convergence [6]. Even improved v-belt models with Coulomb friction still have convergence issues [12].

The EPP friction force per unit length is described by:

$$f(s) = \begin{cases} k_f u(s), & u(s) < \frac{\mu n(s^*)}{k_f} \\ \mu n(s), & u(s) \geq \frac{\mu n(s^*)}{k_f} \end{cases} \tag{1}$$

where k_f is the EPP spring stiffness, μ is the coefficient of friction, $n(s)$ is the normal force per unit belt length, and $u(s)$ is the axial belt displacement. At some point, the belt displacement exceeds $\frac{\mu n(s^*)}{k_f}$, and the friction changes from EPP to Coulomb friction. This point is called the transition point and is denoted by s^*.

The EPP friction force is dependent on the axial belt displacement, as seen in Figure 12. This EPP friction model can be made to approach Coulomb's Law by an appropriate choice of the EPP spring constant. The situation depicted in Figure 12 assumes uni-directional micro/macro slip as can be expected in steady belt drive operation. The situation with displacement reversals is more complicated, and can cause a hysteresis effect [4].

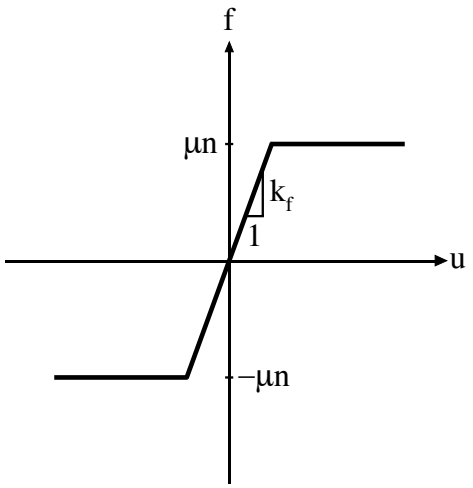

Figure 12: Elastic/Perfectly-Plastic Friction Model.

2.2 Flat Belt System with EPP Friction

Figure 13 shows a two-pulley, flat belt drive where the driver and driven pulleys have equal radii, R. The analysis presented here can be extended to a general belt drive with different pulley radii, but we examine the equal-size pulley to streamline the discussion. The angular coordinate, ϕ_i, is attached to the pulley and is measured from the belt entry points on the pulley. The subscripts, $i = 1, 2$, denote the driven and driver pulleys, respectively. An Eulerian formulation is employed such that arclength coordinate, $s_i = R\phi_i$, is fixed in space. A uniform, axially-moving flat belt wraps around the rotating pulleys, and experiences axial displacement, $u_i(s, t)$. When the belt first enters the pulley at $s_i = 0$, the EPP spring is unstretched. The belt loses contact with the pulley at $s_i = s_f$, and because of the geometry of the flat belt, $s_f = R\pi$.

To streamline the development of theory, the remainder of this section will discuss the derivations for the driven pulley, and the 1 and 2 subscripts will be dropped. However, the analysis presented can easily be extended to the driver pulley. For the driven pulley, the belt enters the pulley with low tension, T_L, and velocity, v_L. It then leaves the pulley with high tension, T_H, and corresponding velocity, v_H.

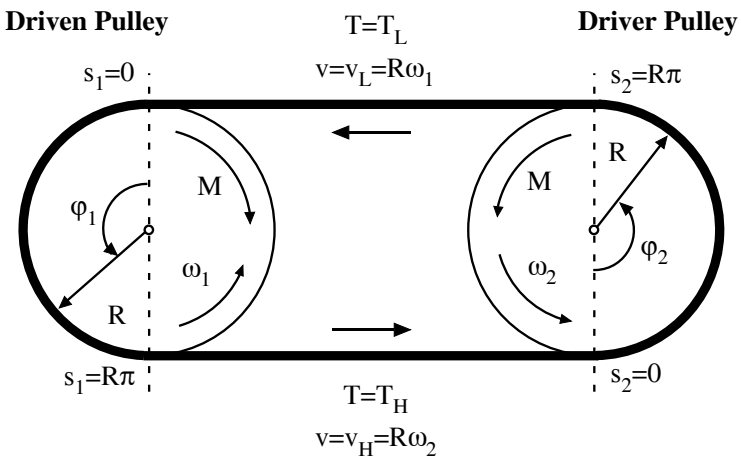

Figure 13: Two Pulley Belt Drive System.

A linear, constitutive law relates the belt tension, T, to the belt strain, ϵ, by:

$$T = EA\epsilon \tag{2}$$

where E is Young's Modulus and A is the cross-sectional area of the belt. Because the belt is assumed to be linearly elastic, the tension distribution can be separated into two components:

$$T = T_o + EA\hat{\epsilon} \tag{3}$$

where $\hat{\epsilon}$ is the incremental strain of the belt element and T_o is a reference initial tension at the pulley inlet. Similarly, the strain can also be decomposed approximately into:

$$\epsilon = \epsilon_o + \hat{\epsilon} \tag{4}$$

where ϵ_o is the strain at the inlet, and the additional strain of the belt element, $\hat{\epsilon}$, is related to the displacement by:

$$\hat{\epsilon} = \frac{\partial u}{\partial s} \tag{5}$$

The initial tension, T_o, is given by:

$$T_o = T_L - EA\frac{\partial u}{\partial s}(0) \tag{6}$$

It will become evident later no solutions can be found such that $T_o = T_L$ and where T_L is the tension when the belt enters the driven pulley.

2.2.1 Kinematics

To find the velocity of the belt as it traverses the driven pulley, $v(s)$, it is assumed that the belt enters the pulley with velocity v_L. For a non-rotating observer attached to the pulley, the ϕ coordinate is fixed and the belt makes small displacements as time progresses. As the belt stretches, the belt's velocity is different from the pulley velocity due to a nonzero strain, $\frac{\partial u}{\partial s}$. This difference in speed is accounted for by the material derivative:

$$\frac{Du}{Dt} = \frac{\partial u}{\partial s}\frac{\partial s}{\partial t} + \frac{\partial u}{\partial t} \tag{7}$$

Assume that the velocity of the driven pulley at the belt interface is $v_L = R\omega$, velocity of the s coordinate attached to the pulley is also v_L, and the velocity of the belt element is:

$$v(s) = v_o + \frac{Du}{Dt} = v_o + v_L\frac{\partial u}{\partial s} + \frac{\partial u}{\partial t} \tag{8}$$

where v_o corresponds to the velocity at T_o and

$$v_o = v_L\left(1 - \frac{\partial u}{\partial s}(0)\right) \tag{9}$$

At steady-state, all time derivatives are zero and the velocity of the belt element on the driven pulley is given by:

$$v(s) = v_o + v_L\frac{du}{ds} \tag{10}$$

2.2.2 Equations of Motion

For a system under Coulomb's Law, a steadily rotating belt drive develops a single adhesion and slip zone on each driver and driven pulley. Together, the adhesion and slip zones span the entire belt-pulley contact region [8]. Similar arguments can be made for the case with an EPP friction model. It is assumed there exists a stick zone and a slip, or fully-developed creep, zone as shown in Figure 14. When the belt enters the pulley, it is assumed that the belt is stuck to the pulley and there is a region of constant tension in the stick zone. This stick zone starts at $s = 0$ and ends at $s = s_o$. At $s = s_o$, an additional zone of elastic creep develops as the EPP spring stretches. This elastic creep zone begins as the belt starts to creep along the pulley and its tension increases. In this zone, the friction law is governed

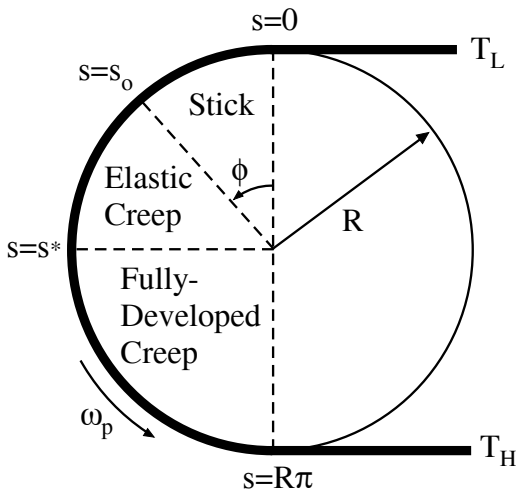

Figure 14: Stick, Elastic Creep and Fully-Developed Creep Zones for a Flat Belt Drive.

by the EPP friction model. The fully-developed creep zone is defined between $s = s^*$ and $s = R\pi$. Here, the EPP spring is stretched to full capacity and the friction force is fully developed. Note that the angles of the sum all zones must equal $s = R\pi$ or $\phi = 180°$

If the belt enters the pulley with zero initial strain, then $T_o = T_L$ and a zone of constant tension can exist. However, it will be shown that the initial strain can never equal to zero and therefore, $T_o \neq T_L$. As a result, no stick zone can exist and the elastic creep zone begins at $s_o = 0$. In (1), the first equation in the EPP friction model indicates that the belt is in the elastic creep zone, and the second equation indicates that the belt in the fully-developed creep, or slip, zone.

2.2.2.1 Hamilton's Principle

To derive the equations of motion, Hamilton's Principle was used. The kinetic and potential energies were derived for the belt in two sections governed by the two functions in the piece-wise EPP friction model. In the first section, described by the subscript, e, the belt is in the elastic creep zone. In the second section, the belt is in the slip zone and is described by the subscript, c. The two sections are separated at the transition angle, s^*. Using the velocity equation in (8), the kinetic energies of the flat belt system are given by:

$$T_e(s,t) = \int_{s_o}^{s^*} \frac{1}{2} m \left(v_o + v_L u_e' + \dot{u}_e\right)^2 ds \tag{11}$$

$$T_c(s,t) = \int_{s^*}^{s_f} \frac{1}{2} m \left(v_o + v_L u_c' + \dot{u}_c\right)^2 ds \tag{12}$$

where $\dot{u} = \frac{\partial u}{\partial t}$ and $u' = \frac{\partial u}{\partial s}$.

The potential energy of the belt in the elastic creep zone is due the axial stiffness, EA, and the EPP spring such that:

$$V_e(s,t) = \int_{s_o}^{s^*} \left\{ \left(T_o u_e' + \frac{1}{2} EA \left(u_e'\right)^2 \right) + \frac{1}{2} k_f (u_e)^2 \right\} ds \tag{13}$$

The potential energy of the belt in the slip zone is only due to the axial stiffness:

$$V_c(s,t) = \int_{s^*}^{s_f} \left(T_o u_c' + \frac{1}{2} EA \left(u_c'\right)^2 \right) ds \tag{14}$$

The non-conservative work due to friction is given by:

$$\delta W_{NC} = -\int_{s^*}^{s_f} \mu n(s) \delta u_c ds \tag{15}$$

Taking the first variation of (11)-(14), yields

$$\delta T_e(s,t) = \int_{s_o}^{s^*} m \left(v_o + v_L u_e' + \dot{u}_e\right) \left(v_L \delta u_e' + \delta \dot{u}_e\right) ds \tag{16}$$

$$\delta T_c(s,t) = \int_{s^*}^{s_f} m \left(v_o + v_L u_c' + \dot{u}_c\right) \left(v_L \delta u_c' + \delta \dot{u}_c\right) ds \tag{17}$$

$$\delta V_e(s,t) = \int_{s_o}^{s^*} \left\{ \left(T_o + EA u_e'\right) \delta u_e' + k_f u_e \delta u_e \right\} ds \tag{18}$$

$$\delta V_c(s,t) = \int_{s^*}^{s_f} \left(T_o + EA u_c'\right) \delta u_c' ds \tag{19}$$

The first variations were substituted into Hamilton's Principle:

$$\int_{t_1}^{t_2} \left(\delta L + \delta W_{NC}\right) dt = 0 \tag{20}$$

where, $\delta L = \delta T - \delta V$, $\delta T = \delta T_e + \delta T_c$ and $\delta V = \delta V_e + \delta V_c$. Using (15) - (19), integrating by parts, and plugging back into Hamilton's Principle yields

$$\int_{t_1}^{t_2}(\delta L+\delta W_{NC})\,dt = \int_{t_1}^{t_2}\Bigg\{-\int_{s_o}^{s^*}\left\{\left(mv_L^2-EA\right)u_e''+2mv_L\dot{u}_e'+m\ddot{u}_e+k_f u_e\right\}\delta u_e ds - \int_{s^*}^{s_f}\left\{\left(mv_L^2-EA\right)u_c''+2mv_L\dot{u}_c'+m\ddot{u}_c+\mu n\right\}\delta u_c ds + \left[\left\{mv_L\left(v_o+v_Lu_e'+\dot{u}_e\right)-\left(T_o+EAu_e'\right)\right\}\delta u_e\right]\Big|_{s_o}^{s^*} + \left[\left\{mv_L\left(v_o+v_Lu_c'+\dot{u}_c\right)-\left(T_o+EAu_c'\right)\right\}\delta u_c\right]\Big|_{s^*}^{s_f}\Bigg\}dt=0 \quad (21)$$

2.2.2.2 Mode Synthesis

A constraint must be enforced to keep the displacements, u_e and u_c, continuous at the transition point, s^*. This holonomic constraint equation relating the generalized coordinates is given by:

$$g=u_e(s^*,t)-u_c(s^*,t)=0 \quad (22)$$

with the first variation:

$$\delta g=\delta u_e(s^*,t)-\delta u_c(s^*,t)=0 \quad (23)$$

Let β be the Lagrange multiplier such that:

$$\int_{t_1}^{t_2}\beta\delta g dt=\int_{t_1}^{t_2}\beta\left[\delta u_e(s^*,t)-\delta u_c(s^*,t)\right]dt=0 \quad (24)$$

Subtracting (24) from (21) yields:

$$\int_{t_1}^{t_2}(\delta L+\delta W_{NC}-\beta\delta g)\,dt = \int_{t_1}^{t_2}\Bigg\{-\int_{s_o}^{s^*}\left\{\left(mv_L^2-EA\right)u_e''+2mv_L\dot{u}_e'+m\ddot{u}_e+k_f u_e\right\}\delta u_e ds - \int_{s^*}^{s_f}\left\{\left(mv_L^2-EA\right)u_c''+2mv_L\dot{u}_c'+m\ddot{u}_c+\mu n\right\}\delta u_c ds + \left[\left\{mv_L\left(v_o+v_Lu_e'+\dot{u}_e\right)-\left(T_o+EAu_e'\right)-\beta\right\}\delta u_e\right]\Big|_{s_o}^{s^*} + \left[\left\{mv_L\left(v_o+v_Lu_c'+\dot{u}_c\right)-\left(T_o+EAu_c'\right)-\beta\right\}\delta u_c\right]\Big|_{s^*}^{s_f}\Bigg\}dt \quad (25)$$

The resulting equations of motion are:

$$m\ddot{u}_e+2mv_L\dot{u}_e'+\left(mv_L^2-EA\right)u_e''+k_f u_e=0, \quad s_o<s<s^* \quad (26)$$

$$m\ddot{u}_c+2mv_L\dot{u}_c'+\left(mv_L^2-EA\right)u_c''+\mu n=0, \quad s^*<s<s_f \quad (27)$$

with natural boundary conditions:

$$\left[\left\{mv_L\left(v_o + v_L u_e' + \dot{u}_e\right) - \left(T_o + EAu_e'\right)\right\}\delta u_e\right]\Big|_{s_o} = 0 \tag{28}$$

$$\left[\left\{mv_L\left(v_o + v_L u_e' + \dot{u}_e\right) - \left(T_o + EAu_e'\right) - \beta\right\}\delta u_e\right]\Big|_{s^*} = 0 \tag{29}$$

$$\left[\left\{mv_L\left(v_o + v_L u_c' + \dot{u}_c\right) - \left(T_o + EAu_c'\right) - \beta\right\}\delta u_c\right]\Big|_{s^*} = 0 \tag{30}$$

$$\left[\left\{mv_L\left(v_o + v_L u_c' + \dot{u}_c\right) - \left(T_o + EAu_c'\right)\right\}\delta u_c\right]\Big|_{s_f} = 0 \tag{31}$$

Because $u_e(s^*)$ and $u_c(s^*)$ can be varied, they are not equal to zero, and the geometric boundary conditions at s^* are not used. The Lagrange multiplier, β, is a constant, and the natural boundary conditions in (29) and (30) are used such that:

$$\beta = mv_L\left(v_o + v_L u_e'(s^*) + \dot{u}_e(s^*)\right) - \left(T_o + EAu_e'(s^*)\right) \tag{32}$$

$$\beta = mv_L\left(v_o + v_L u_c'(s^*) + \dot{u}_c(s^*)\right) - \left(T_o + EAu_c'(s^*)\right) \tag{33}$$

Setting the Lagrange multiplier, β, equal to each other gives:

$$mv_L\left(v_o + v_L u_e'(s^*) + \dot{u}_e(s^*)\right) - \left(T_o + EAu_e'(s^*)\right) = mv_L\left(v_o + v_L u_c'(s^*) + \dot{u}_c(s^*)\right) - \left(T_o + EAu_c'(s^*)\right) \tag{34}$$

Because the displacements are equal for all time, the displacement velocities are equal and $\dot{u}_e(s^*) = \dot{u}_c(s^*)$. Canceling like terms and simplifying, the boundary condition in (34) becomes,

$$u_e'(s^*) = u_c'(s^*) \tag{35}$$

Note that from Equation (3), the tension distribution is linearly related to the strain. Therefore, (35) can be equally expressed as:

$$T_e(s^*) = T_c(s^*) \tag{36}$$

For the boundary condition at $s = s_o$, choose the geometric boundary condition such that,

$$u_e(s_o) = 0 \tag{37}$$

At $s = s_f$, choose the natural boundary condition such that,

$$u_c'(s_f) = \frac{T_o - mv_L v_o}{mv_L^2 - EA} \tag{38}$$

Also, the holonomic constraint in (22) is an additional boundary condition such that

$$u_e(s^*) = u_c(s^*) \tag{39}$$

2.2.2.3 Linearization

The resulting equations of motion in (26) and (27) were linearized around a steady-state configuration such that,

$$u(s,t) = \bar{u}(s) + \tilde{u}(s,t) \tag{40}$$

where, $\tilde{u}(s,t)$ denotes small perturbations about the equilibrium, $\bar{u}(s)$. It is assumed that the transition point, s^*, is unaffected by the small perturbations in displacement, $\tilde{u}(s,t)$. The first derivatives of (40) in time and space are:

$$\dot{u}(s,t) = \dot{\tilde{u}}(s,t) \tag{41}$$

$$\ddot{u}(s,t) = \ddot{\tilde{u}}(s,t) \tag{42}$$

$$\dot{u}'(s,t) = \dot{\tilde{u}}'(s,t) \tag{43}$$

$$u'(s,t) = \bar{u}'(s) + \tilde{u}'(s,t) \tag{44}$$

$$u''(s,t) = \bar{u}''(s) + \tilde{u}''(s,t) \tag{45}$$

Equations (40) and (45) were substituted into the equations of motion in (26) and (26). The equilibrium solutions governed by $\bar{u}(s)$ and the equations of motion governed by $\tilde{u}(s,t)$ were separated. Suppressing the tilde ($\sim$) notation, the linearized equations of motion around the equilibrium solutions for the two regions are:

$$m\ddot{u}_e + 2mv_L\dot{u}_e' + \left(mv_L^2 - EA\right)u_e'' + k_f u_e = 0, \quad 0 < s < s^* \tag{46}$$

$$m\ddot{u}_c + 2mv_L\dot{u}_c' + \left(mv_L^2 - EA\right)u_c'' + \frac{\mu}{R}\left(EAu_c{}'\right) = 0, \quad s^* < s < s_f \tag{47}$$

Similarly, Equations (40) and (45) were substituted into the boundary conditions. Because the equilibrium solutions already satisfy the boundary conditions from the equations of motion,

$$u_e\left(s_o, t\right) = 0 \tag{48}$$

$$\frac{\partial u_c}{\partial s}\left(s_f, t\right) = 0 \tag{49}$$

The other homogeneous boundary conditions are:

$$u_e\left(s^*, t\right) - u_c\left(s^*, t\right) = 0 \tag{50}$$

$$\frac{\partial u_e}{\partial s}\left(s^*, t\right) - \frac{\partial u_c}{\partial s}\left(s^*, t\right) = 0 \tag{51}$$

The equilibrium displacement solutions, $\bar{u}_e$ and $\bar{u}_c$, are governed by:

$$\left(mv_L^2 - EA\right)\bar{u}_e'' + k_f\bar{u}_e = 0, \quad s_o < s < s^* \tag{52}$$

$$\left(mv_L^2 - EA\right)\bar{u}_c'' + \mu n = 0, \quad s^* < s < s_f \tag{53}$$

Rearranging the equilibrium solutions in (52) and (53) yields:

$$\bar{u}_e'' = \frac{k_f\bar{u}_e}{\left(EA - mv_L^2\right)}, \quad s_o < s < s^* \tag{54}$$

$$\bar{u}_c'' = \frac{\mu n}{\left(EA - mv_L^2\right)}, \quad s^* < s < s_f \tag{55}$$

These equations are the same as in previous studies that use the momentum balance of the belt element in the tangential and normal directions to get the following equations [1]:

$$\frac{d}{ds}T(s) - G\frac{d}{ds}v(s) = f(s) \tag{56}$$

$$n(s) = \frac{T(s) - Gv(s)}{R} \tag{57}$$

where $f(s)$ is the EPP friction model given by (1) and $G = mv_L$ is the mass flow rate. By taking the spatial derivative of (3) and (10) and substituting into (56), the momentum balance in the tangential direction can be expressed as a second degree ordinary differential equation of the displacement, $u(s)$:

$$u'' = \frac{f(s)}{EA - Gv_L} \tag{58}$$

To preserve continuity between the EPP and Coulomb regions, the boundary conditions for the equilibrium solutions in (54) and (55) obtained from the Hamilton's Principle are:

$$u_e(s_o) = 0 \tag{59}$$

$$u_e(s^*) = u_c(s^*) \tag{60}$$

$$T_e(s^*) = T_c(s^*) \tag{61}$$

To fully constrain the system, three other boundary conditions are enforced through the assumptions made at beginning of this section. From the EPP friction model, continuity of the friction force must be enforced at the transition point, such that:

$$k_f u_e(s^*) = \frac{\mu}{R} T_c(s^*) \tag{62}$$

Two other boundary conditions constrain the tension distribution to the desired tension difference:

$$T_e(s_o) = T_L \tag{63}$$

$$T_c(s_f) = T_H \tag{64}$$

Using the equilibrium solutions in (54) and (55) with the boundary conditions in (59)-(64), s^* and T_o were found in closed form using Maple. The solutions are functions of the belt and system parameters, as well as the low and high tensions, T_L and T_H. From Maple, it was determined that $\frac{du}{ds}(0)$ never equals zero, and so $T_o \neq T_L$. This implies that solutions where the initial strain is zero will not yield a result. This condition is unlike previous analysis.

The Maple worksheet created to find the closed-form solutions to s^* and T_o for the driven pulley is found in Appendix A. For the driver pulley, the tension boundary conditions at the inlet and exit are simply switched such that

$$T_e(s_o) = T_H \tag{65}$$

$$T_c(s_f) = T_L \tag{66}$$

Also, because the direction of displacement is reversed, the coefficient of friction is now $\mu = -1.2$, as previous shown in Figure 12. The Maple worksheet to find the closed-form solutions to s^* and T_o for the driver pulley is found in Appendix B.

2.2.3 Stability Analysis

Because this system is nonlinear, there may exist multiple solutions. Also, there is no guarantee that those solutions are stable. To determine the stability of the nonlinear equilibrium solution, a local stability analysis can be performed. We will first assume that the solution is separable and the response is harmonic. Then, the solutions are of the form:

$$u_e(s,t) = \Psi(s)e^{i\omega_n t}, \qquad s_o < s < s^* \tag{67}$$

$$u_c(s,t) = \Phi(s)e^{i\omega_n t}, \qquad s^* < s < s_f \tag{68}$$

where ω_n are the frequencies of oscillation. The eigenvalues are $\lambda_n = i\omega_n$ and the eigenfunctions for the EPP friction and Coulomb friction regions are $\Psi(s)$ and $\Phi(s)$, respectively.

Substituting (67) and (68) into the equations of motion in (46) and (47) and using the boundary conditions in (48) and (51), leads to the homogeneous boundary value problem:

$$\left(mv_L^2 - EA\right)\frac{d^2\Psi}{ds^2} + 2mv_L i\omega\frac{d\Psi}{ds} + \left(k_f - m\omega^2\right)\Psi(s) = 0, \quad s_o < s < s^* \tag{69}$$

$$\left(mv_L^2 - EA\right)\frac{d^2\Phi}{ds^2} + \left(2mv_L i\omega + \frac{\mu}{R}EA\right)\frac{d\Phi}{ds} + \left(-m\omega^2\right)\Phi(s) = 0, \quad s^* < s < s_f \tag{70}$$

with boundary conditions of:

$$\Psi\left(s_o\right) = 0 \tag{71}$$

$$\frac{d\Phi}{ds}\left(s_f\right) = 0 \tag{72}$$

$$\Psi\left(s^*\right) - \Phi\left(s^*\right) = 0 \tag{73}$$

$$\frac{d\Psi}{ds}\left(s^*\right) - \frac{d\Phi}{ds}\left(s^*\right) = 0 \tag{74}$$

Using (69)-(74), the eigenfunctions, $\Psi(s)$ and $\Phi(s)$, and oscillation frequencies, ω_n, were found using Maple and is displayed in Appendix C. Because axially-moving systems are inherently gyroscopic, the eigenvalues and the corresponding eigenfunctions occur in complex conjugates [18, 19]. Unlike nongyroscopic undamped linear systems, these complex eigenfunctions do not pass through equilibrium simultaneously. The eigenfunction for the entire arclength is a piecewise function given by:

$$\Pi(s) = \begin{cases} \Psi(s), & s < s^* \\ \Phi(s), & s \geq s^* \end{cases} \tag{75}$$

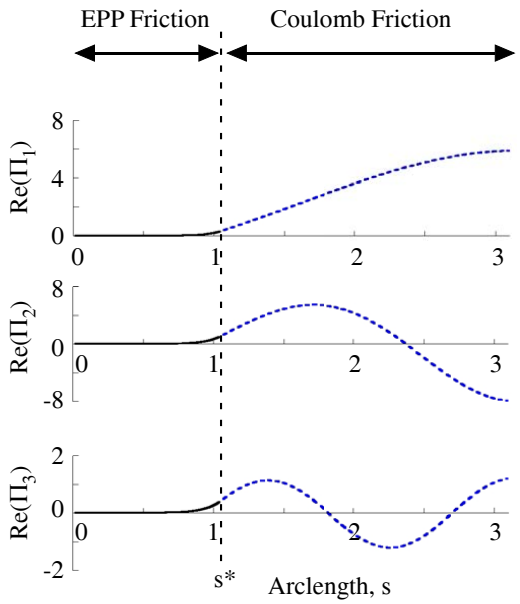

Figure 15: Plot of Real Part of the First Three Eigenfunctions.

Finally, the displacements of the axially-moving flat belt are:

$$u_e(s,t) = \Psi(s)e^{i\omega_n t} + \overline{\Psi}(s)e^{-i\bar{\omega}_n t}, \quad s_o < s < s^* \tag{76}$$

$$u_c(s,t) = \Phi(s)e^{i\omega_n t} + \overline{\Phi}(s)e^{-i\bar{\omega}_n t}, \quad s^* < s < R\pi \tag{77}$$

where u_e and u_c are real-valued functions.

Assuming that the lower eigenvalues are more likely to be less stable, the higher frequencies are neglected. The first three eigenfunctions, $\Pi_1(s)$, $\Pi_2(s)$, and $\Pi_3(s)$, are plotted in Figure 15 as a function of arclength.

Similar to Wickert [29], the critical transport speed for this axially moving system is:

$$v_{cr} = \left(\frac{EA}{m}\right)^{1/2} \tag{78}$$

When the velocity is less than the critical transport speed, v_{cr}, the system is positive definite. The real parts of these complex eigenvalues are negative and the solutions are stable.

Table 1: Physical Properties of Example Flat Belt Drive for BVP Solver.

Parameter	Assigned Value
ρ	1036 kg/m^2
A	0.0001 m^2
E	800680 kN/m^2
ω_2	120 rad/s
μ	1.2
R	0.08125 m
k_f	8.1x10^7 N/m^2

2.3 Results and Comparisons

2.3.1 Boundary Value Problem Results

Given that the stability of the nonlinear system has been established, the two-pulley belt drive shown in Figure 13 can be analyzed further. To compare the EPP friction model to Coulomb's Law, results for both friction laws were generated. The low tension is kept constant at 200 N and the high tension is varied from 400 N to 4000 N. Other parameters are shown in Table 1. For the EPP friction model, the equilibrium solutions in (54) and (55) along with the boundary conditions in (59)-(64) were solved using the bvp4c solver in MATLAB. The solutions to a flat belt system with Coulomb's Law is well known and is not reviewed here. However, material on Coulomb's Law for flat belt drives can be reviewed in [8].

The friction forces on the driven and driver pulleys for both the Coulomb and EPP friction models are shown in Figures 16 and 17. Both models have slope discontinuities at the transition points separating the two different zones. For the results with Coulomb's Law, the slope discontinuity occurs at the transition point between the stick and slip zones. For the results with the EPP friction model, the slope discontinuity occurs between the elastic creep and fully-developed creep zones. For the EPP friction model and low tension difference, there are initially only elastic creep zones where the friction force gradually increases from zero at the entry points. As the high tension increases, the elastic creep zone gets smaller and the friction forces in the elastic creep zone increases. For the Coulomb friction model, the stick zone decrease with increase in high tension. Ultimately, as high tension keeps increasing, the adhesion arc approaches zero and effectively only the slip zone

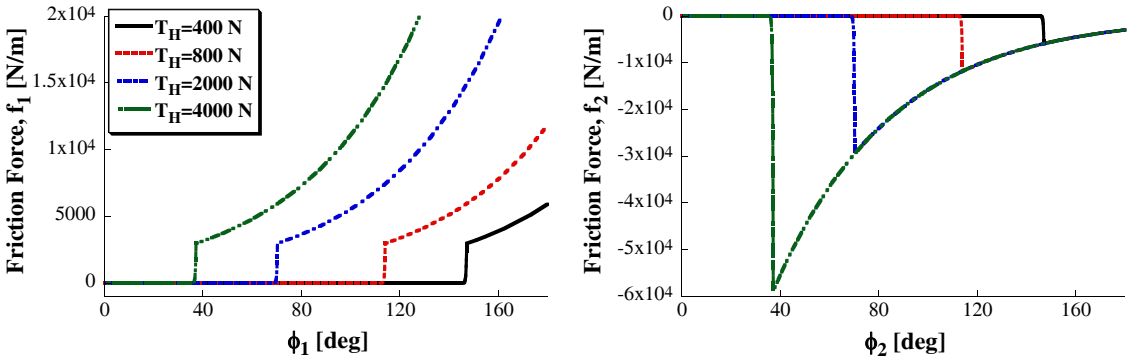

(a) Driven Pulley. (b) Driver Pulley.

Figure 16: Friction Force with Coulomb Friction.

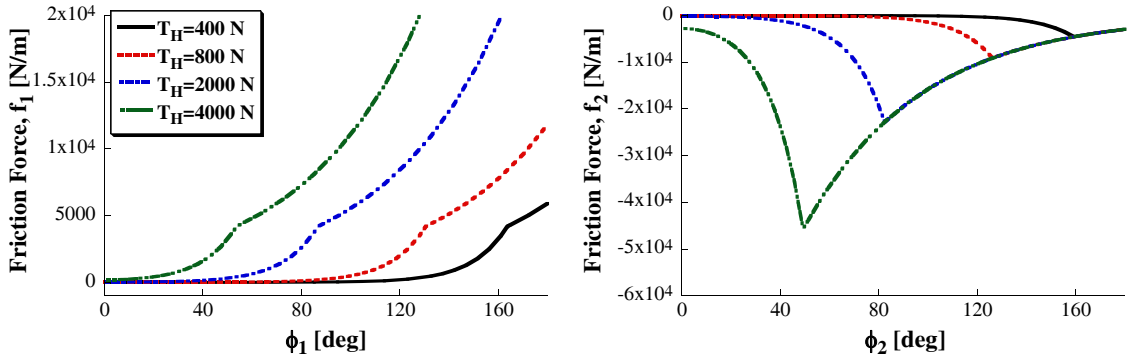

(a) Driven Pulley. (b) Driver Pulley.

Figure 17: Friction Force with Elastic/Perfectly-Plastic Friction.

exists in the entire arc of the pulley.

The belt tension on the driven and driver pulleys for both friction models are shown in Figures 18 and 19. The tension distribution for both friction models are continuous, but with discontinuous slope for the Coulomb friction and smoothly varying for the EPP friction model. The elimination of these slope discontinuities can potentially alleviate parameter sensitivities for complex models such as the v-belt for continuously variable transmissions.

As seen in the Figures 17 and 19, the elastic creep and slip zones vary with the tension difference. To study how they vary, the transition angle, ϕ^*, and the slip angle, ϕ_s, was calculated for both the driven and driver pulleys as a function of the high tension, T_H, as shown in Figure 20. The low tension was kept constant again at 200 N and the same parameters in Table 1 were used. To calculate the transition angles, the closed-form equations

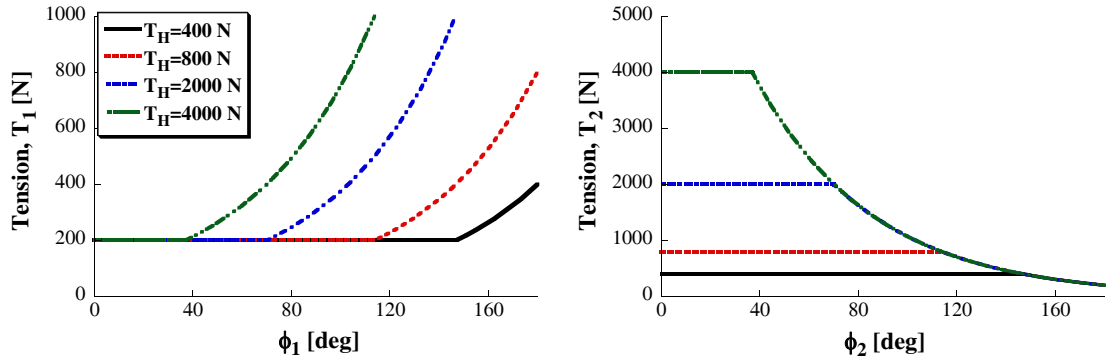

(a) Driven Pulley. (b) Driver Pulley.

Figure 18: Tension with Coulomb Friction.

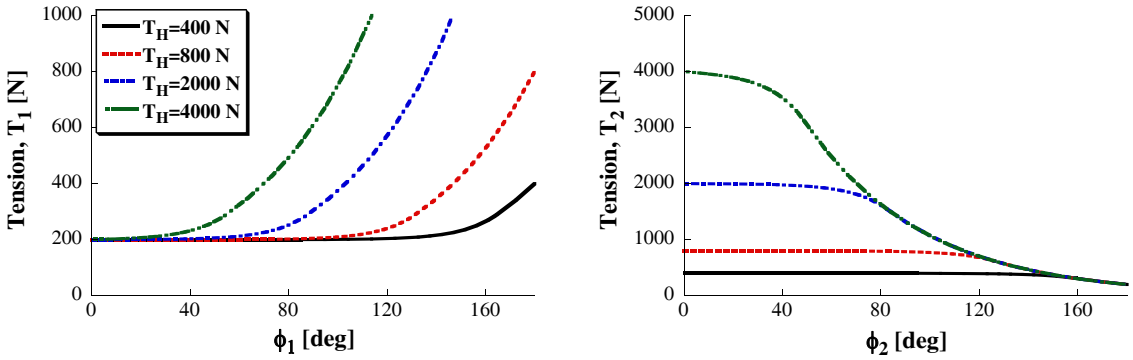

(a) Driven Pulley. (b) Driver Pulley.

Figure 19: Tension with Elastic/Perfectly-Plastic Friction.

from the Maple codes in Appendix A and B were used.

As shown in Figure 20, the transition angles and slip angles are not the same for both pulleys. For a certain high tension, the elastic creep arc is larger on the driven pulley than on the driver pulley. The transition angle is 180° at a high tension of 380 N for the driven pulley. This means that only a elastic creep zone exists on the entire arc of the pulley. For the driver pulley, the transition angle is 180° at $T_H = 310$ N. However, because the minimum high tension for the driven pulley was higher than 310 N, the driver pulley can never have only an elastic creep zone along the entire arc of the pulley. The driver pulley will always have a slip arc.

As the high tension increases, the transition angle decreases. This means that the elastic creep zone decreases and the slip zone increases. The sum of ϕ^* and ϕ_s must equal 180°

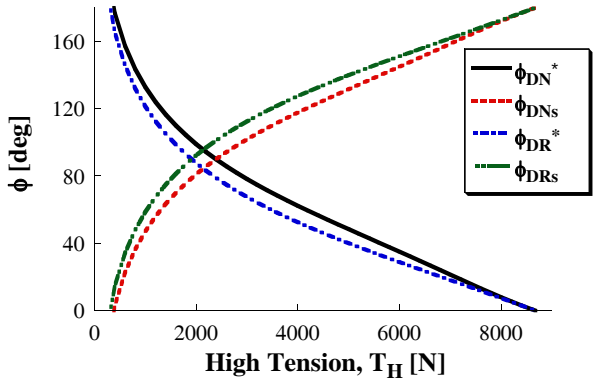

Figure 20: Transition and Slip Angle as a Function of High Tension, T_H.

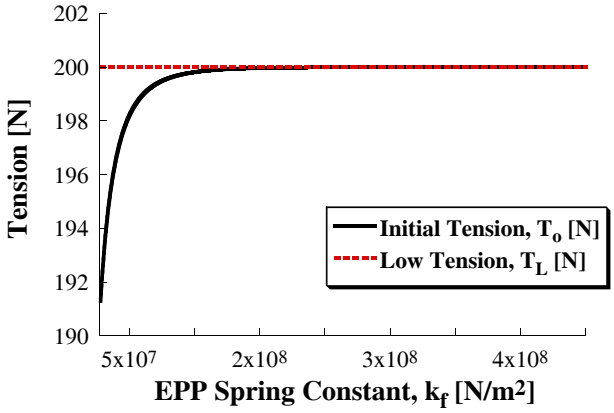

Figure 21: Initial Tension, T_o as a Function of EPP Spring Constant, k_f.

as discussed in Section 2.2.2. At a high tension of approximately 2390 N, the elastic creep zone and the fully-developed creep zone have equal arcs at 90° for the driven pulley. At a high tension of 8674 N, the slip arc for both pulleys is 180° and the fully-developed creep zone is the only zone that exists on the entire arc of the pulley.

For a given set of parameters, the only parameter we can vary is the EPP spring stiffness. To fully understand the behavior of the initial tension, T_o, and initial strain, $\frac{du}{ds}(0)$, they were plotted as a function of the EPP spring stiffness, as shown in Figures 21 and 22. As k_f increases, the initial tension converges to the low tension and the initial strain goes to zero. However, when Figure 22 is zoomed in, the initial strain never equals zero but comes very close, shown in Figure 23.

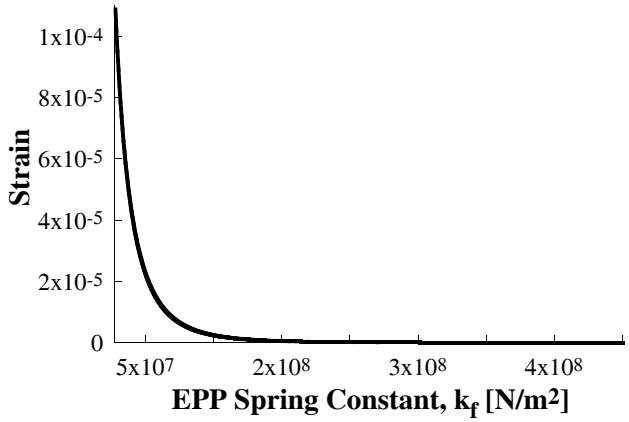

Figure 22: Initial Strain, $\frac{du}{ds}(0)$, as a Function of EPP Spring Constant, k_f.

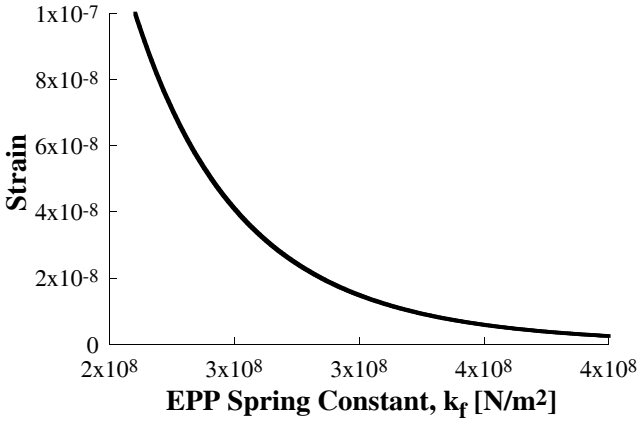

Figure 23: Reduced Axis of Initial Strain, $\frac{du}{ds}(0)$, as a Function of EPP Spring Constant, k_f.

Table 2: Additional Properties and Results of Example Flat Belt Drive.

Parameter	Assigned Value	Parameter	$k_f = 2.8\text{x}10^7$	$k_f = 2.0\text{x}10^8$	$k_f = 8.1\text{x}10^9$
M	45 N-m	T_L	156.2 N	155.1 N	158.3 N
ω_2	120 rad/s	T_H	712.2 N	716.7 N	707.1 N
l_o	0.01 m	ω_1	119.1 rad/s	119.1 rad/s	119.1 rad/s
k	150 kN/m^2	ϕ^*_{DN}	3.14 rad	2.16 rad	1.93 rad
		ϕ_{DN_s}	0 rad	0.98 rad	1.21 rad
		ϕ^*_{DR}	2.34 rad	2.08 rad	1.93 rad
		ϕ_{DR_s}	0.80 rad	1.06 rad	1.21 rad
		T_o	146.4 N	155.1 N	158.3 N
		$\frac{du}{ds}(0)$	$1.2\text{x}10^{-4}$	$2.5\text{x}10^{-7}$	~ 0

2.3.2 Finite Element Model Results

Next, to verify the accuracy of the boundary value problem, it was compared to a finite element model. The finite element model is an extended version of the one developed in [15]. Added to the finite element model is an additional state variable that was included to keep track of the axial belt displacement and evaluate the friction forces. In the finite element model, the driver pulley maintains a constant angular velocity of 120 rad/s, and the driven pulley was given a constant opposing torque of 45 N-m. The same parameters in Table 1 was used and other parameters for the finite element model are shown Table 2. Additional information about this finite element model can found in [15]. Results were generated for three different values of the EPP spring constant, k_f: $k_f = 2.8\text{x}10^7$, $k_f = 2\text{x}10^8$, and $k_f = 8.1\text{x}10^9$ N/m^2. These three values of the EPP spring constant were chosen specifically to explore the reasonable operating range and their specific values will be explained in the following paragraphs.

The resulting tensions, T_L and T_H, as well as the angular velocity of the driven pulley, ω_1, were calculated as outputs from the finite element model. The values of T_L, T_H, and ω_1 are shown in Table 2 for each of the three values of k_f. These values were used as input parameters to the analytical model so that direct comparisons could be made. The equilibrium solutions, (54) and (55), and the boundary conditions in (59)-(64) were solved with a boundary value problem solver in MATLAB. A comparison of forces predicted by the analytical model and the finite element model for the three values of k_f is shown in

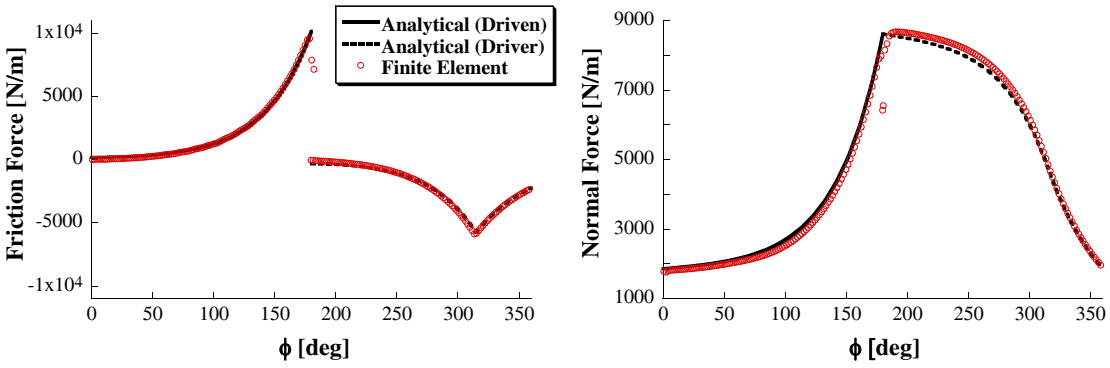

Figure 24: Analytical and Finite Element Predicted Friction and Normal Forces Per Unit Length with Minimum $k_f = 2.8\text{x}10^7$ N/m^2.

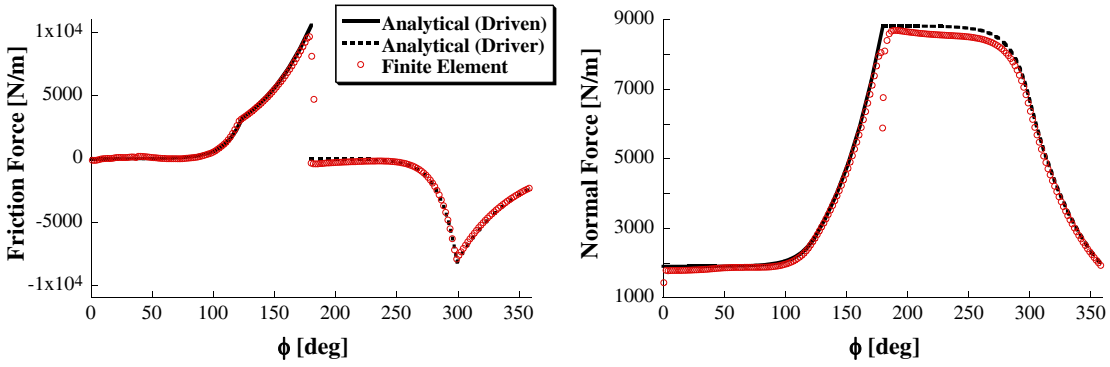

Figure 25: Analytical and Finite Element Predicted Friction and Normal Forces Per Unit Length with $k_f = 2\text{x}10^8$ N/m^2.

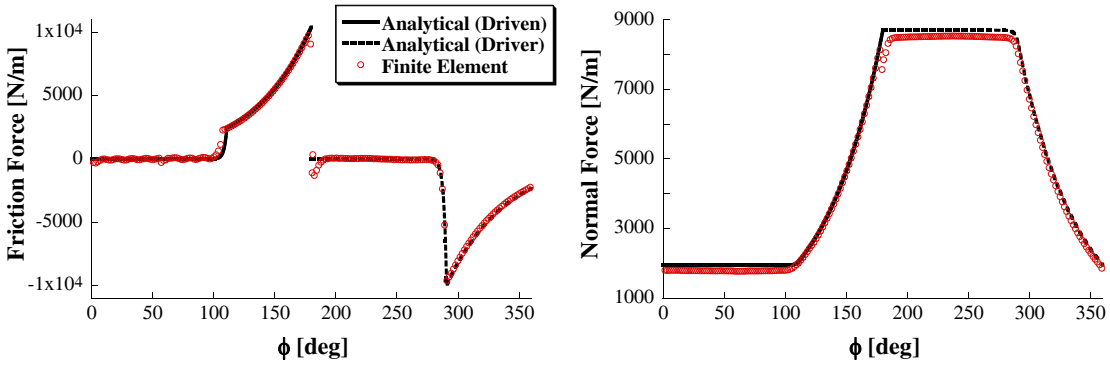

Figure 26: Analytical and Finite Element Predicted Friction and Normal Forces Per Unit Length with $k_f = 8.1\text{x}10^9$ N/m^2.

Figures 24 through 26. The friction force and normal force per unit length are plotted for both the driven and driver pulleys. The angle, ϕ, in Figures 24 through 26 begins with $\phi = 0°$ corresponding to the inlet of the driven pulley. The inlet of the driver pulley starts at $\phi = 180°$.

Figure 24 shows the analytical and finite element results with $k_f = 2.8\text{x}10^7$ N/m^2. This is the minimum value of k_f allowable so that the system undergoes the prescribed tension change within the entire pulley arc. When $s^* = R\pi$, the belt undergoes elastic creep throughout the entire pulley surface. If k_f is smaller than this minimum value, then the system cannot undergo the prescribed tension change and the boundary conditions are not preserved. This minimum value of k_f can be determined by solving the equilibrium equations with the boundary conditions:

$$T(0) = T_L \tag{79}$$

$$T(R\pi) = T_H \tag{80}$$

$$u(0) = 0 \tag{81}$$

$$k_f u_e(R\pi) = \frac{\mu}{R} T_H \tag{82}$$

The Maple worksheet used to find this minimum k_f is shown in Appendix C.

Figure 25 shows the results with an intermediate EPP spring constant of $k_f = 2\text{x}10^8$ N/m^2 and a slip angle of about 0.98 rad. It is apparent from Figure 12 that as k_f increases, the EPP model can be made to approach the Coulomb friction law and s^* goes to $R\phi_s$, where ϕ_s is the slip angle given in [8]. As k_f, increases the EPP spring stiffness becomes large and can be approximated as rigid. This near-Coulomb solution is shown in Figure 26 where the slip zone begins at $\phi^* = 1.93$ rad (110.6°) and the slip angle is $\phi_s = 1.21$ rad (69.4°). This slip angle for $k_f = 81\text{x}10^8$ N/m^2 is close to the approximated value of 1.24 rad given in [8]. Like Coulomb's Law, the solution in Figure 26 has a sharp change in slope at the transition angle. One objective of the EPP friction model was to smooth the sharp changes from the results. If the EPP spring constant is too large, then the benefits of the elasticity of the EPP friction model is lost. Therefore, the EPP spring stiffness must be

chosen appropriately such that the belt can still undergo the prescribed tension change, but also not too large that sharp changes in slope appears at the transition point.

In Figures 24-26, the analytical model matches very well with the results generated from the finite element model. For all values of k_f, the friction forces have slope discontinuities at the transition points between zones. However, in Figures 24 and 25, the normal distribution is slope continuous. The removal of slope discontinuities in the normal and tension distributions will alleviate parameter sensitivities for complex models such as the v-belt for continuously variable transmissions.

The transition and slip angles, initial tension, T_o, and the initial strain, $\frac{du}{ds}(0)$, for each of the three EPP spring stiffness were also displayed in Table 2. From the table, it is evident that as the EPP spring stiffness increases, the initial tension converges to the low tension, T_L, and the initial strain goes to zero.

2.4 Summary

In this chapter, the Elastic/Perfectly-Plastic friction model was developed and applied to a two-pulley flat belt system with equal pulley radii. The equations of motion for a thin flat belt engaging a pulley were developed using Hamilton's Principle. Solution to these equations is difficult because of the piece-wise linear nature of the governing partial differential equations. At steady-state, the solution to the governing equations is composed of a "fully-slipping" or "perfectly-plastic" region (on the high-tension side), which is adjacent to another region that has elastic deformation of the belt at the belt/pulley interface. It was found that, for belt velocities below the critical speed, there is one steady-state solution where the elastic deformation region begins immediately at the initial point of contact of the belt with the pulley.

The stability of the steady-solutions was examined using a linearized set of governing equations. The stability of the perturbations to the steady-solutions was determined from an eigenvalue/eigenvector analysis. It was found that the steady-state solution was stable.

For low EPP spring constants, it was found that the initial strain in the belt was not zero. However, as the EPP spring constant increased, the initial strain did reduce to nearly

zero and the initial tension converged to the prescribed low tension. A minimum value for the EPP spring constant was also calculated for a specific set of parameters such that only an elastic creep zone exists on the entire arc of the driven pulley. However, the driver pulley cannot have only an elastic creep arc and a fully-slipping zone always exists along surface of the driver pulley.

Comparison of results using the analytical model developed in this chapter to results predicted by a dynamic finite element model show excellent agreement. It was found that if the EPP spring stiffness is too small, then the belt cannot undergo the prescribed tension change. On the other hand, if the value for the EPP spring stiffness is too large, then the EPP model approaches Coulomb's Law and sharp changes appear at the transition angle. Therefore, the EPP spring stiffness must be chosen appropriately such that the belt can still undergo the prescribed tension change, but also not so large that sharp changes in slope appear at the transition point.

It was found that the EPP model had no slope discontinuities in the normal force. However, the results with Coulomb's Law did produce slope discontinuities in the normal force. The elimination of these slope discontinuities could potentially help alleviate convergence issues for more complex models. Furthermore, inclusion of a physically motivated elastic creep region into more complicated systems, such as v-belts, may result in the development of models having greater numerical stability. Therefore, the Elastic/Perfectly-Plastic friction model was applied to a v-belt system. In the next chapter, the governing equations for a v-belt system with equal pulley radii are derived and the results are discussed.

CHAPTER III

THE EPP FRICTION LAW FOR V-BELT ANALYSIS

In this chapter, the Elastic/Perfectly-Plastic friction law is applied to a v-belt system. The governing equations for a v-belt system are derived and the results are compared to the model with Coulomb's Law.

3.1 V-Belt System with EPP Friction

To investigate the implementation and usefulness of the EPP friction model on complex systems, it is applied to the two-pulley v-belt system with equal pitch radii, R, as shown in Figure 27. The analysis presented in this chapter can be extended in a straight-forward manner to a more general belt system with different size pulleys. The angular coordinate, ϕ_i, begins when the belt enters the pulley. The subscripts, $i = 1, 2$, will again denote the driven and driver pulleys, respectively. The driver pulley has a constant angular velocity of ω_2. The belt-pulley contact points, $C_1 \sim C_4$, are not known *a priori* and must be determined in the analysis.

Figure 28 shows a cross-section of the v-belt and the pulley groove. The angle of the groove wedge is β, and in this analysis, β is the same for both pulleys. The belt radius coordinate, $r(s)$, is determined by:

$$r(s) = R - x \tag{83}$$

where, x is the belt radial displacement. The belt radial displacement is given by [6]:

$$x = R - r(s) = \frac{2p_z}{k} \tag{84}$$

where, p_z is the pressure load component exerted on the belt along the pulley axial direction and k is the radial spring stiffness. The radial spring stiffness is determined primarily by the belt cross-sectional geometry and material properties. Gerbert and Sorge approximate this relationship by:

$$k = 12\frac{H}{B}E_z \tan\beta \tag{85}$$

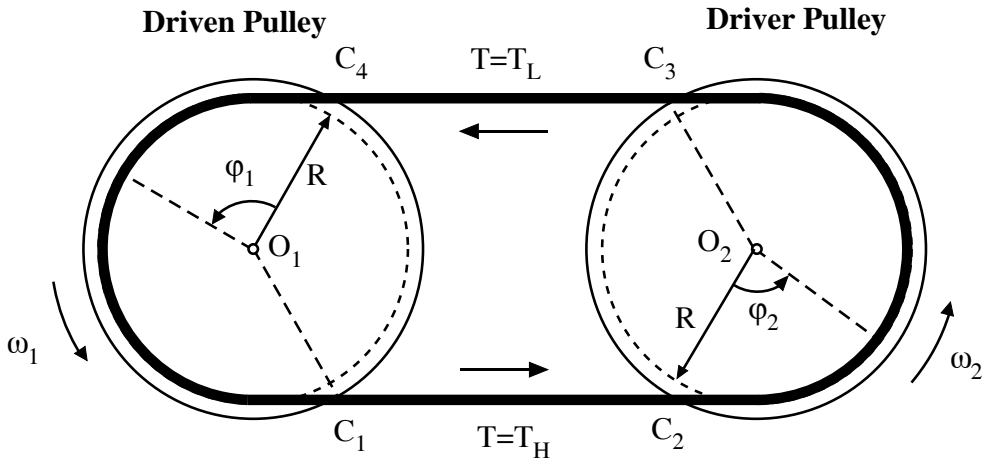

Figure 27: Two Pulley V-Belt System.

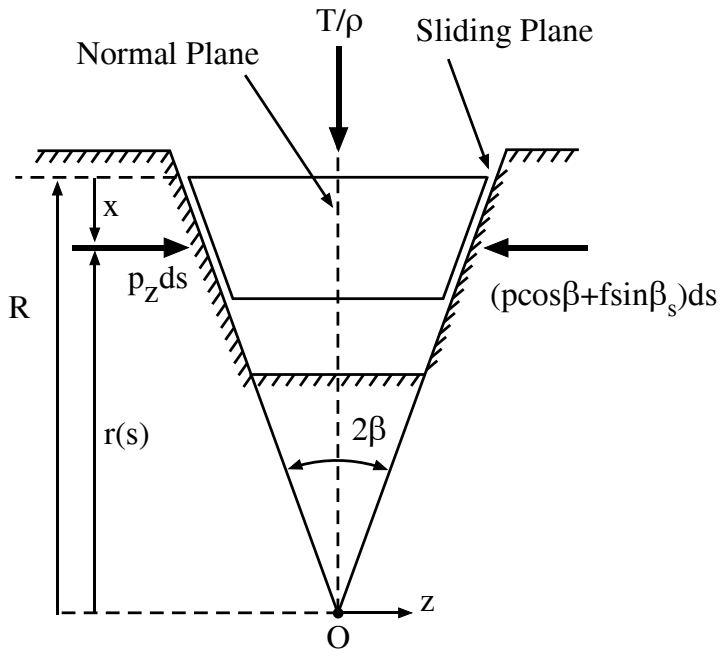

Figure 28: Cross-Section of V-Belt and Pulley Groove.

where, H is the belt height, B is the belt width (top side of v-belt), and E_z is the belt modulus of elasticity in the transverse direction.

From geometry, the pressure, p_z, can be expressed as:

$$p_z = p\cos\beta + f(s)\sin\beta_s \tag{86}$$

where, $f(s)$ is the Elastic/Perfectly-Plastic friction model governed by:

$$f(s) = \begin{cases} k_f u(s), & u(s) < \frac{\mu}{k_f} p_c(s^*) \\ \mu p_c(s), & u(s) \geq \frac{\mu}{k_f} p_c(s^*) \end{cases} \tag{87}$$

where, s^* is the transition coordinate at which the friction changes from elastic creep to slip. Similar to the flat belt model, the belt is in the elastic creep zone when the displacement is less than $\frac{\mu}{k_f} p_c(s^*)$, and the belt is in the fully-developed creep, or slip, zone when the displacement is greater than $\frac{\mu}{k_f} p_c(s^*)$.

Plugging (86) into (84) yields:

$$x = \frac{2}{k}\left(p(s)\cos\beta + f(s)\sin\beta_s\right) \tag{88}$$

Solving for the pressure with the appropriate friction force from (87) yields:

$$p_e(s) = \frac{\frac{1}{2}kx - k_f u_e(s)\sin\beta_s}{\cos\beta} \tag{89}$$

$$p_c(s) = \frac{kx}{2\cos\beta + 2\mu\sin\beta_s} \tag{90}$$

where, p_e is the pressure in the elastic creep zone and p_c is the pressure in the slip zone. The resulting pressure distribution is a piecewise function given by:

$$p(s) = \begin{cases} p_e(s), & u(s) < \frac{\mu}{k_f} p_c(s^*) \\ p_c(s), & u(s) \geq \frac{\mu}{k_f} p_c(s^*) \end{cases} \tag{91}$$

3.1.1 Kinematics

Friction develops on the sliding plane between the belt and pulley interface and the relative sliding velocity vector, $\boldsymbol{V}_s$, exists in the sliding plane, as shown in Figure 29. The direction of the sliding velocity vector is given by the sliding angle, γ. The z-component of the belt-relative sliding velocity vector, $\boldsymbol{V}_s$, is

$$(V_s)_z = V_s\sin\beta_s \tag{92}$$

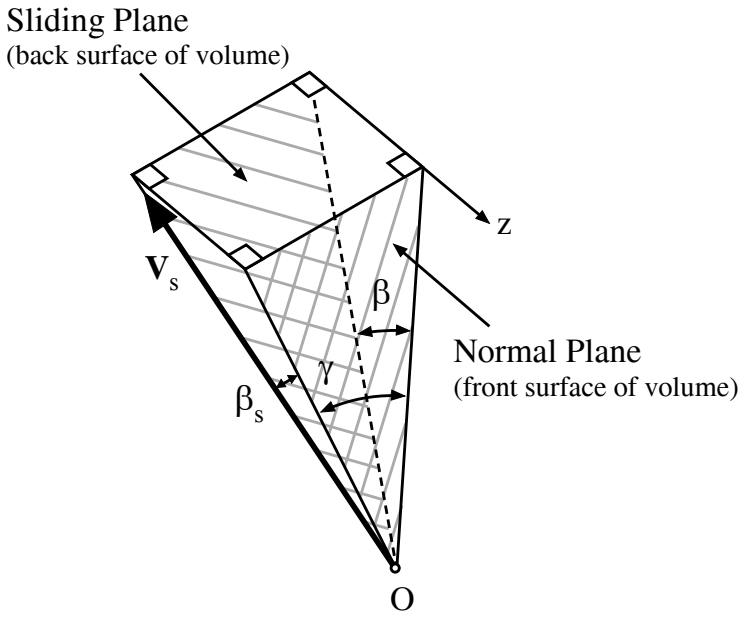

Figure 29: Geometry of Sliding and Normal Planes.

where, β_s is the angle between the relative sliding velocity vector, $\boldsymbol{V}_s$, and the normal plane. From Figure 29, $(V_s)_z$ can also be written as:

$$(V_s)_z = V_s \cos\beta_s \cos\gamma \tan\beta \tag{93}$$

By equating (92) and (93), and then eliminating the $(V_s)_z$ term leads to a relationship governing β_s:

$$\tan\beta_s = \tan\beta \cos\gamma \tag{94}$$

where, $-(\pi/2) \leq \tan\beta_s \leq \pi/2$.

Figure 30 shows the velocity vectors for an element of the v-belt. The point O indicates the center of the pulley. The angular velocity of the pulley is ω and the velocity of the belt element is V. At radius, r, the velocity of the pulley is $r\omega$. The two expressions relating the velocity, V, and sliding velocity, V_s, are:

$$V\cos\theta = r\omega + V_s \sin\gamma \tag{95}$$

$$V\sin\theta = V_s \cos\gamma \tag{96}$$

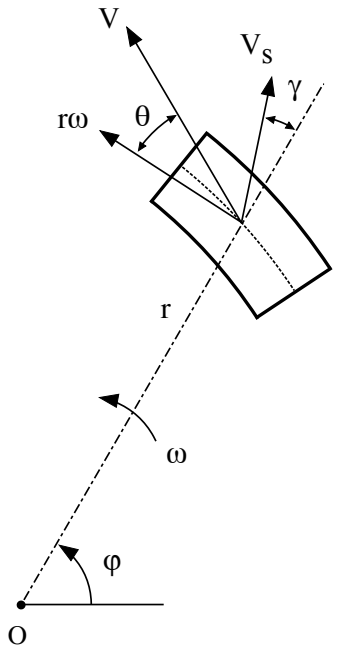

Figure 30: Velocity Vectors for an Element of V-Belt.

where, θ is the inclination angle between the belt velocity and the velocity of the pulley. Eliminating V_s from the above two equations and using the relationship in (83), gives an expression governing the sliding angle, γ:

$$\tan\gamma = \frac{\cos\theta - (R-x)\omega\left(EAm_o - G^2\right)/[G(F+EA)]}{\sin\theta} \tag{97}$$

where, $F = T - GV$ is the tractive tension, T is the belt tension, $G = m_o V$ is the mass flow rate, EA is the longitudinal stiffness, and m_o is the belt mass density per unit length. For steady motions, the conservation of mass requires that G be constant. The mass flow rate is not known initially and must be determined during the analysis.

3.1.2 Governing Equations

Figure 31 shows the free body diagram for an element of the v-belt when it is sliding in the pulley groove. In this chapter, the v-belt is modeled as a axially-moving string. O is the center of the pulley, and Q is the center of curvature of the belt. Balancing the linear momentum in the tangential and normal directions yields:

$$\frac{d(T-GV)}{ds} = 2[-p(s)\sin\beta\sin\theta + f(s)\cos\beta_s\sin(\theta+\gamma)] \tag{98}$$

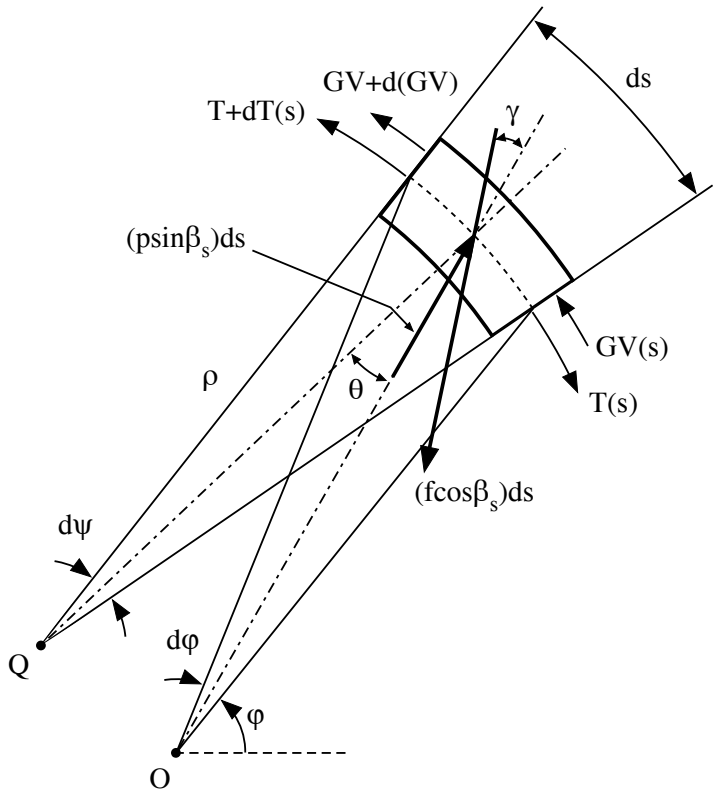

Figure 31: Free Body Diagram of an Element of V-Belt.

$$\frac{T - GV}{\rho} = 2[p(s)\sin\beta\cos\theta - f(s)\cos\beta_s\cos(\theta+\gamma)] \tag{99}$$

where, $p(s)$ is the normal compressive pressure governed by (91), $f(s)$ is the friction force governed by (87), and ψ is the natural angular coordinate.

3.1.3 Geometry

The natural coordinates of (98) and (99) are (s, ψ), as shown in Figure 31. These natural coordinates must be converted to polar coordinates (r, ϕ) to describe the belt as it traverses around the circular pulley. From Figure 31, the following geometric relations can be derived:

$$ds = \frac{r d\phi}{\cos\theta} \tag{100}$$

$$\rho = \frac{ds}{d\psi} \tag{101}$$

$$d\psi = d\phi - d\theta \tag{102}$$

$$\tan\theta = \frac{dr}{rd\phi} = \frac{r'}{r} \tag{103}$$

where, ρ is the belt radius of curvature.

Substitution of (83), and (100)-(102) into the equilibrium equations in (98), (99), and (103), leads to the polar-coordinate based equations:

$$\frac{dF}{d\phi} = 2[-p\sin\beta\sin\theta + f\cos\beta_s\sin(\theta+\gamma)]\frac{R-x}{\cos\theta} \tag{104}$$

$$\frac{d\theta}{d\phi} = 1 - \frac{2}{F}[p\sin\beta\cos\theta - f\cos\beta_s\cos(\theta+\gamma)]\frac{R-x}{\cos\theta} \tag{105}$$

$$\frac{dx}{d\phi} = -(R-x)\tan\theta \tag{106}$$

A constitutive law can be used to relate the belt tension, T, to the belt velocity, V. From [1, 23, 10, 13], the constitutive law is:

$$T = EA\left(m_o V/G - 1\right) \tag{107}$$

or,

$$F = \left(EAm_o - G^2\right)V/G - EA \tag{108}$$

Similar to the flat belt formulation in Chapter 2, the constitutive equation relating the tension to the strain is given by:

$$T(s) = T_o + EA\frac{du}{ds} \tag{109}$$

Equation (109) can be rearranged to form a differential equation governing the displacement. Using the geometric relations in (83), and (100) - (102), the polar-based equation for the displacement is given by:

$$\frac{du}{d\phi} = \frac{(T(s)-T_o)}{EA}\frac{(R-x)}{\cos\theta} \tag{110}$$

In this chapter, we will let $T_o = T_L$ to directly compare with the results from Kong and Parker's model.

The angular coordinate of the driven and driver pulleys, ϕ_1 and ϕ_2, begin when the belt enters the pulleys. Because of seating and unseating, the wrap angles of the belt-pulley contact zones are unknown. This is because, unlike the flat belt, the wrap angle is not always 180°, as illustrated in Figure 32. The seating and unseating phenomenon allows for

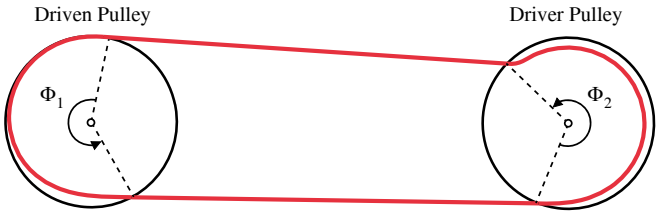

Figure 32: V-Belt Seating and Unseating.

wrap angles to exceed 180°. The wrap angles of the driven and driver pulley are not known *a priori* and are determined during the analysis. The wrap angles for the driven and driver pulleys, Φ_1 and Φ_2, can be used to define nondimensional variables:

$$\hat{\phi}_1 = \frac{\phi_1}{\Phi_1} \tag{111}$$

$$\hat{\phi}_2 = \frac{\phi_2}{\Phi_2} \tag{112}$$

where, $0 < \hat{\phi}_1, \hat{\phi}_2 < 1$.

Therefore, the governing differential equations for the belt on the driven pulley are:

$$\frac{dF_1}{d\hat{\phi}_1} = 2[-p_1 \sin\beta \tan\theta_1 + f_1 \cos\beta_{s1}(\tan\theta_1 \cos\gamma_1 + \sin\gamma_1)](R - x_1)\Phi_1 \tag{113}$$

$$\frac{d\theta_1}{d\hat{\phi}_1} = \left\{1 - \frac{2}{F_1}[p_1 \sin\beta - f_1 \cos\beta_{s1}(\cos\gamma_1 - \sin\gamma_1 \tan\theta_1)](R - x_1)\right\}\Phi_1 \tag{114}$$

$$\frac{dx_1}{d\hat{\phi}_1} = -(R - x_1)\tan\theta_1 \Phi_1 \tag{115}$$

$$\frac{du_1}{d\hat{\phi}_1} = \frac{(T_1 - T_o)}{EA}\frac{(R - x_1)}{\cos\theta}\Phi_1 \tag{116}$$

To solve for the unknown, but constant, wrap angle, Φ_1, a trivial differential equation is incorporated into the boundary value problem:

$$\frac{d\Phi_1}{d\hat{\phi}_1} = 0 \tag{117}$$

where, $0 < \hat{\phi}_1 < 1$.

Similarly, the governing equations for the driver pulley are:

$$\frac{dF_2}{d\hat{\phi}_2} = 2[-p_2 \sin\beta \tan\theta_2 + f_2 \cos\beta_{s2}(\tan\theta_2 \cos\gamma_2 + \sin\gamma_2)](R - x_2)\Phi_2 \tag{118}$$

$$\frac{d\theta_2}{d\hat{\phi}_2} = \left\{1 - \frac{2}{F_2}[p_2 \sin\beta - f_2 \cos\beta_{s2}(\cos\gamma_2 - \sin\gamma_2 \tan\theta_2)](R - x_2)\right\}\Phi_2 \tag{119}$$

$$\frac{dx_2}{d\hat{\phi}_2} = -(R - x_2)\tan\theta_2\Phi_2 \tag{120}$$

$$\frac{du_2}{d\hat{\phi}_2} = \frac{(T_2 - T_o)}{EA}\frac{(R - x_2)}{\cos\theta}\Phi_2 \tag{121}$$

$$\frac{d\Phi_2}{d\hat{\phi}_2} = 0 \tag{122}$$

where, $0 < \hat{\phi}_2 < 1$. Note that the differential equations in (113)-(116) and (118)-(121) are coupled.

Boundary conditions are determined such that the tension distribution is constrained by:

$$T(\phi_i) = T_i \tag{123}$$

$$T(\phi_f) = T_f \tag{124}$$

where, T_i and T_f can be the low or high tensions depending on the pulley.

When the v-belt enters the pulley, the belt radial displacement is zero. Also, when the v-belt leaves the pulley, the belt undergoes unseating and the radial displacement decreases to zero. Therefore, two boundary conditions for the radial displacement are given by:

$$x(\phi_i) = 0 \tag{125}$$

$$x(\phi_f) = 0 \tag{126}$$

The final boundary condition is similar to that of the flat-belt formulation. It is assumed that when the belt enters the pulley, the displacement is zero. Therefore, the last boundary condition is given by:

$$u(\phi_i) = 0 \tag{127}$$

To summarize, the boundary conditions for the driven pulley are:

$$T_1(0) = T_L, \quad T_1(1) = T_H \tag{128}$$

$$x_1(0) = 0, \quad x_1(1) = 0 \tag{129}$$

$$u_1(0) = 0 \tag{130}$$

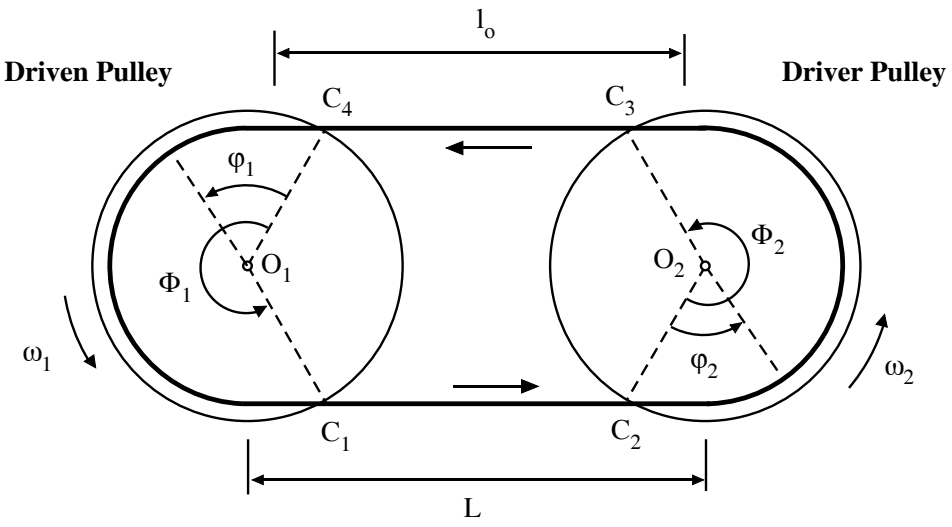

Figure 33: Two Pulley V-Belt System Parameters.

and the boundary conditions for the driver pulley are:

$$T_2(0) = T_H, \quad T_2(1) = T_L \tag{131}$$

$$x_2(0) = 0, \quad x_2(1) = 0 \tag{132}$$

$$u_2(0) = 0 \tag{133}$$

In the above analysis, the low tension span length, l_o, the mass flow rate, G, and the driven pulley rotational speed, ω_1, are unknown, as shown in Figure 33. These three constants are determined during the analysis by adding three additional trivial differential equations:

$$\frac{dl_o}{d\hat{\phi}_1} = 0, \quad \frac{dG}{d\hat{\phi}_1} = 0, \quad \frac{d\omega_1}{d\hat{\phi}_1} = 0 \tag{134}$$

The states of the belt are T_1, T_2, θ_1, θ_2, x_1, x_2, u_1, u_2. These states are governed by the differential equations in (113)-(116) and (118)-(121). The boundary conditions for these differential equations are found in (128)-(133). Constants to solve for are Φ_1, Φ_2, l_o, G_1, and ω_1. These variables are governed by the trivial differential equations in (117), (122), and (134). Other variables are f_1, f_2, p_1, p_2, β_{s1}, β_{s2}, γ_1, γ_2. These can be obtained directly by using Equations (87), (89)-(91), (94), and (97). Additional information for solving this model can be found in [12].

Table 3: Physical Properties of Example V-Belt Drive.

Parameter	Assigned Value
β	18°
m_o	0.108 kg/m^4
EA	120 kN
k	900 kN/m^3
L	1.3933 m
ω_2	1000 pm
μ	0.4
R	0.25 m
k_f	8.1x10^6 N/m^2
T_L	200 N

To get the differential equations to converge, the boundary value problem must start with low parameters. Then, when a solution can be found, that solution is used as the initial guess for a new numerical simulation attempt, and the parameters are slowly increased at the next iteration until the desired value is reached. This method is called the continuation method [24]. For example, if the desired value for EA is 12000 N, then the solution procedure might start with a value of only 2000 N. The algorithm would then increase EA by a small factor and use the solution of the previous iteration as the initial guess for the current iteration. If the difference between the first iteration is too large, then convergence may fail. Therefore, some parameters may required increments by a factor as small as 1.0001 at each iteration. If a factor of 1.001 is used instead, then convergence may fail.

3.2 Results and Comparisons with Previous Work

The differential equations derived in the previous sections solved for the belt tension, T, the belt inclination angle, θ, the belt radial displacement, x, and the belt axial displacement, u. To compare our predictions with previous results from Kong and Parker, the same parameter values from their work in [12] were used. These values are shown in Table 3. The low tension, T_L, was kept constant at 200 N and the high tension, T_H, was varied. The continuation method was used to find the maximum possible high tension was found. For both Coulomb's Law and the EPP friction model, the largest value of T_H was 7781.2 N.

Figures 34 and 35 show the belt tension for the driven and driver pulleys, T_1 and T_2, with Coulomb's Law and the EPP model, respectively. From these figures, it is apparent that

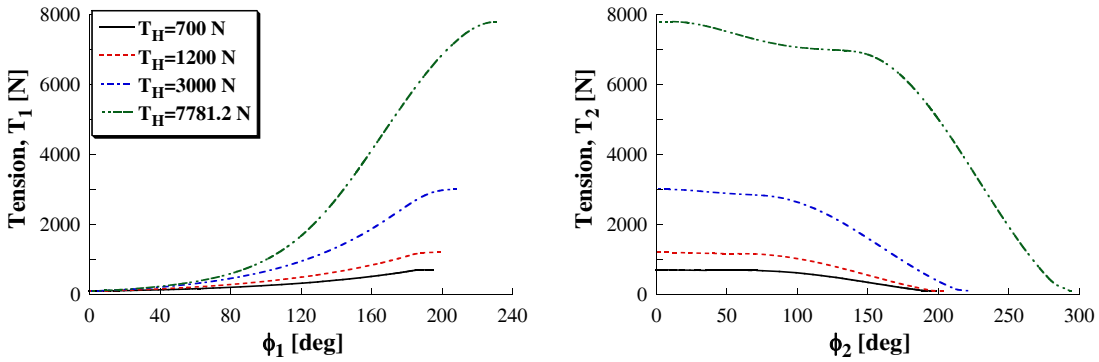

(a) Driven Pulley. (b) Driver Pulley.

Figure 34: Belt Tension with Coulomb Friction.

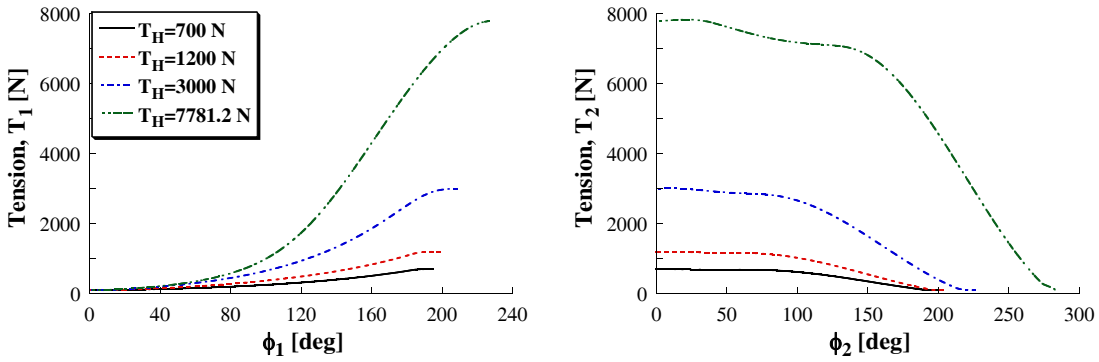

(a) Driven Pulley. (b) Driver Pulley.

Figure 35: Belt Tension with Elastic/Perfectly-Plastic Friction.

there is no significant difference between the Coulomb friction and the Elastic/Perfectly-Plastic friction solutions. This shows that the solutions with EPP friction matches the well-studied and accepted solution with Coulomb's Law. For the driver pulley, the tension stays relatively constant around the high tension, then quickly drops to the prescribed low tension. This indicates that as the tension span increases, the belt undergoes a great amount of stress during the rapid change in tension. This type of operating condition could fatigue the belt material and decrease the life of the v-belt. Therefore, the results in Figures 34 and 35 indicate problematic operating conditions that should be avoided.

Figures 36 and 37 show the belt inclination angle for the driven and driver pulleys, θ_1 and θ_2, with Coulomb's Law and the EPP model, respectively. When the belt inclination angle is zero, the velocity vectors of the belt and pulley are in the same direction. For low tension spans, the inclination angle is zero for much of the belt-pulley contact arc. When

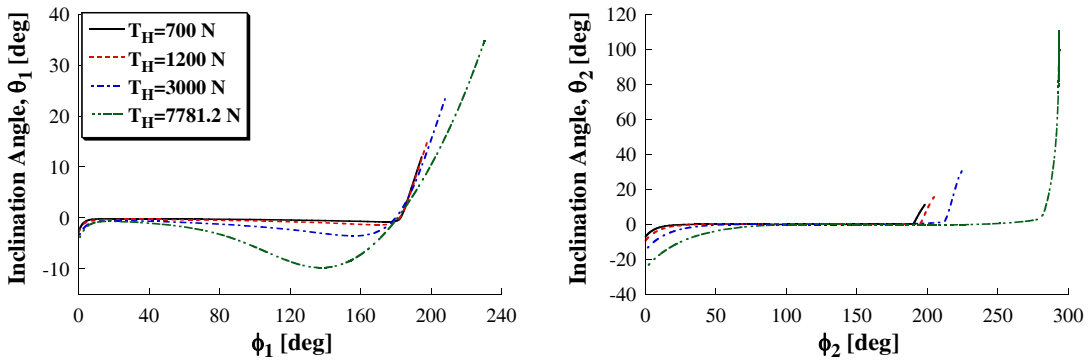

(a) Driven Pulley. (b) Driver Pulley.

Figure 36: Belt Inclination Angle with Coulomb Friction.

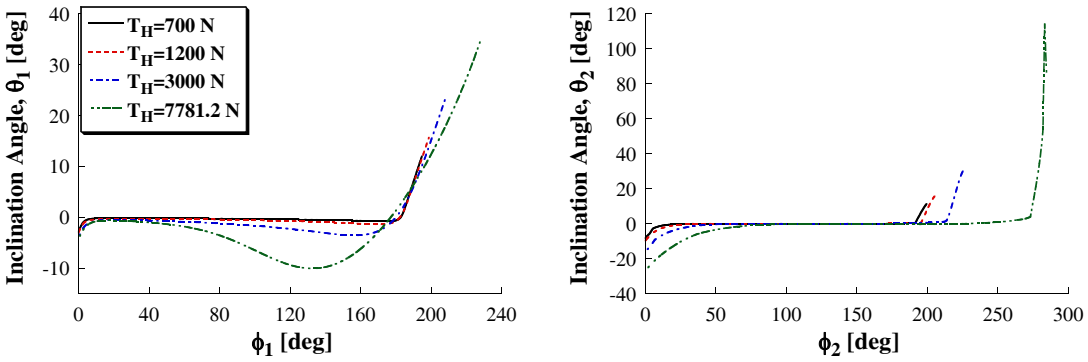

(a) Driven Pulley. (b) Driver Pulley.

Figure 37: Belt Inclination Angle with Elastic/Perfectly-Plastic Friction.

the belt leaves the pulley, the inclination angle increases as the belt unseats in the pulley groove. For large tension spans, the sharpness of the change in inclination angle is smoothed at the exit of the driven pulley, but it is more drastic at the exit of the driver pulley. For low tension spans, sharp changes in inclination angle appear as the belt exits the driven pulley. The sharpness in change of this parameter at the exit of the driver pulley for high tension spans and driven pulley for low tension spans is a cause of convergence failure. Because the sharp changes occur at the exit of the pulley, the belt is in the slip zone and the elasticity of the EPP friction model has no smoothing effect.

Figures 38 and 39 show the belt radial displacement for the driven and driver pulleys, x_1 and x_2, with Coulomb's Law and the EPP model, respectively. The belt radial displacement indicates how much the belt is seating into the pulley grooves, while the belt inclination angle shows the angle of belt relative to the pulley. For both driven and driver pulleys, the

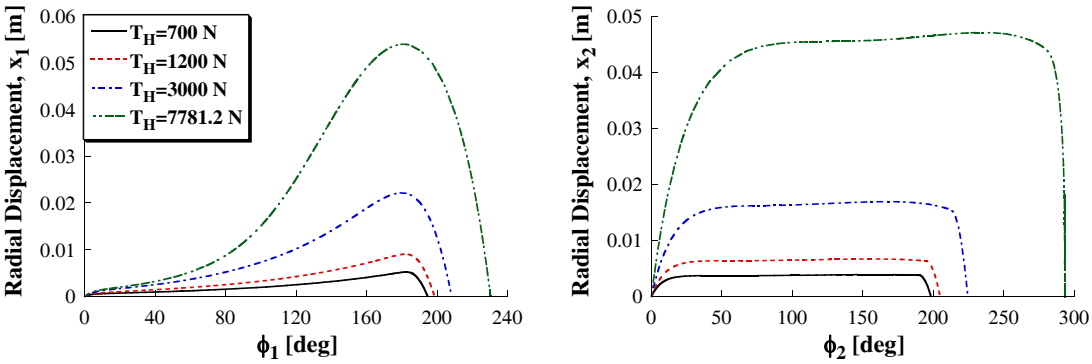

(a) Driven Pulley. (b) Driver Pulley.

Figure 38: Belt Radial Displacement, x, with Coulomb Friction.

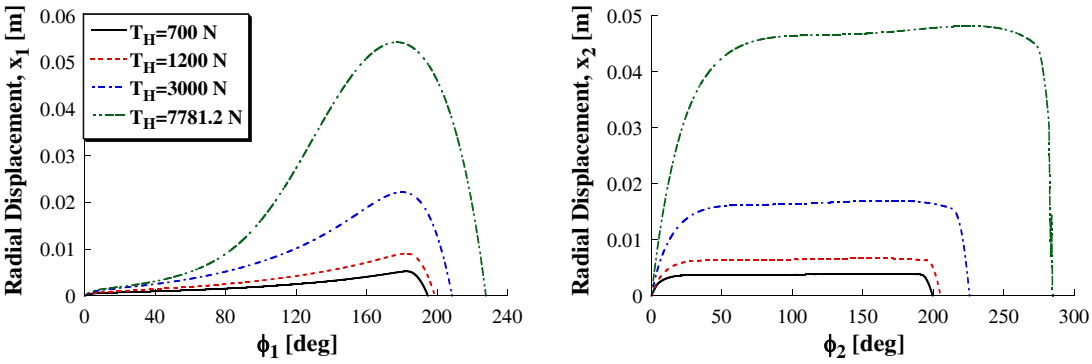

(a) Driven Pulley. (b) Driver Pulley.

Figure 39: Belt Radial Displacement, x, with Elastic/Perfectly-Plastic Friction.

radial displacement is very large at high tension spans. As the belt exits the pulleys, the belt undergoes rapid unseating from the pulley groove. This would put a great amount of stress on the belt and create wear on the belt, decreasing the life of the belt. Such extreme operating conditions should be avoided.

A more physical representation of the belt inclination angle and radial displacement are shown graphically in Figure 40. This figure show how the belt displaces radially into the pulley grooves as the difference between the high and low tensions increase. The belt system shown in Figure 40(d) is a very extreme case and may not be physically possible in real systems, because of possible belt derailing.

Figure 41 shows the belt axial displacement for the driven and driver pulleys, u_1 and u_2, with the EPP friction model. As the belt tension increases, the belt axial displacements also increase. Because the wrap angles are larger for larger tension spans, the belt has more

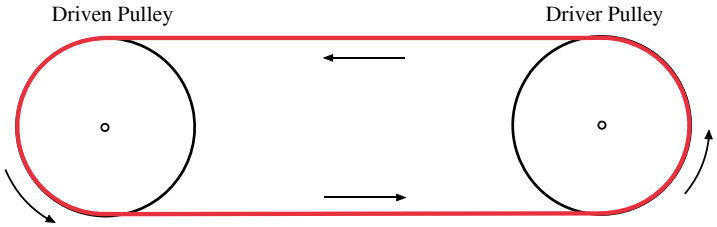

(a) $T_H = 700$ N.

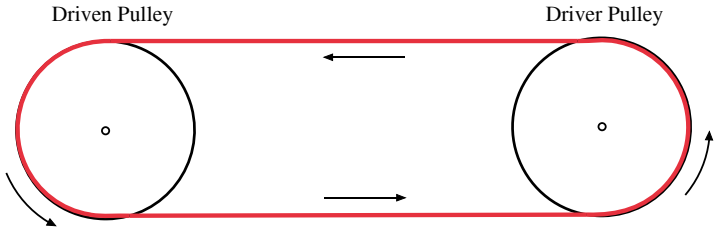

(b) $T_H = 1200$ N.

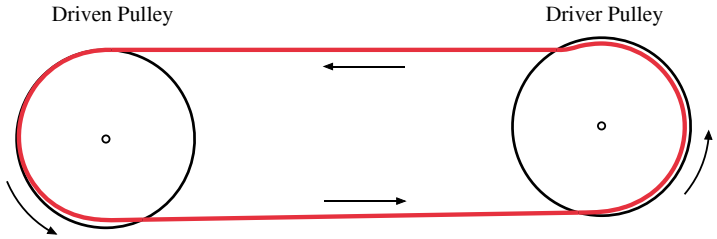

(c) $T_H = 3000$ N.

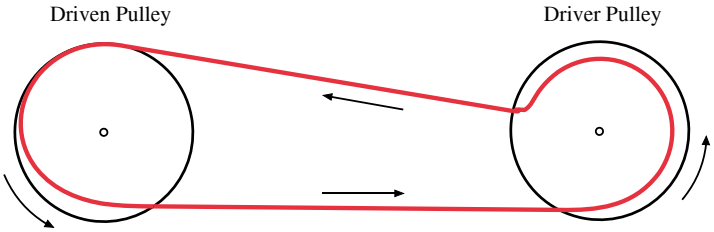

(d) $T_H = 7781.2$ N.

Figure 40: Steady-State Solutions with Elastic/Perfectly-Plastic Friction.

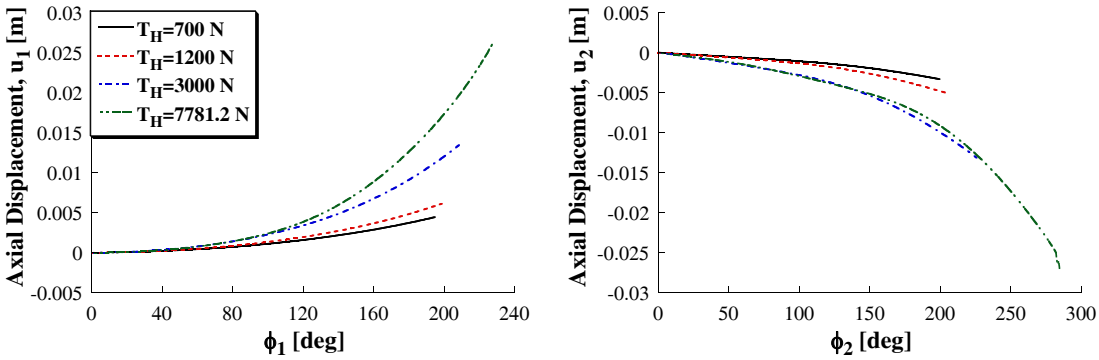

(a) Driven Pulley. (b) Driver Pulley.

Figure 41: Belt Axial Displacement, u, with Elastic/Perfectly-Plastic Friction.

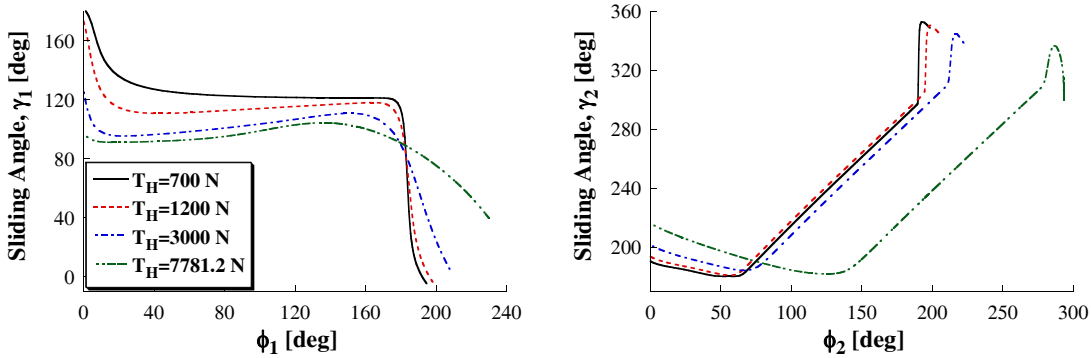

(a) Driven Pulley. (b) Driver Pulley.

Figure 42: Sliding Angle, γ, with Coulomb Friction.

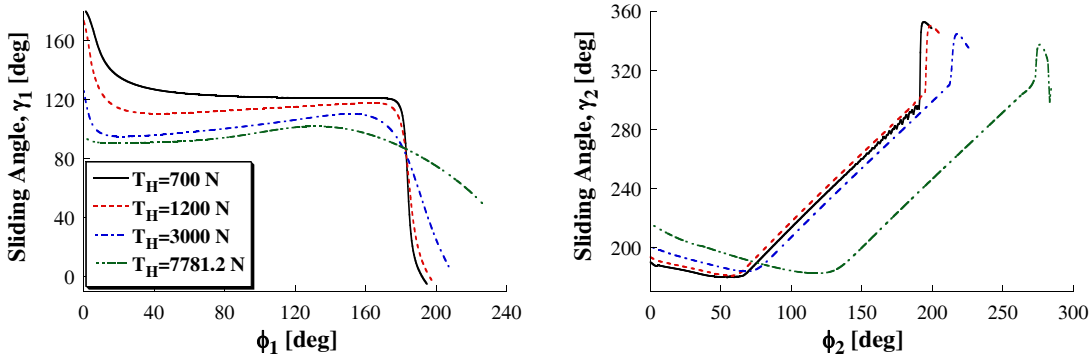

(a) Driven Pulley. (b) Driver Pulley.

Figure 43: Sliding Angle, γ, with Elastic/Perfectly-Plastic Friction.

Table 4: Results From Example V-Belt Drive with Coulomb Friction.

Parameter	Value			
T_H	700 N	1200 N	3000 N	7781.2 N
ω_1	102.7 rad/s	100.4 rad/s	87.1 rad/s	30.9 rad/s
G	2.8 kg-m/s^2	2.7 kg-m/s^2	2.6 kg-m/s^2	2.2 kg-m/s^2
Φ_1	194.7°	198.6°	208.4°	230.4°
Φ_2	198.3°	204.8°	224.4°	293.8°

Table 5: Results From Example V-Belt Drive with EPP Friction.

Parameter	Value			
T_H	700 N	1200 N	3000 N	7781.2 N
ω_1	102.7 rad/s	100.4 rad/s	86.9 rad/s	16.9 rad/s
G	2.8 kg-m/s^2	2.7 kg-m/s^2	2.6 kg-m/s^2	2.2 kg-m/s^2
Φ_1	194.8°	198.8°	208.6°	227.8°
Φ_2	199.5°	205.1°	225.6°	284.5°

time to undergo greater displacement.

The sliding angle for the driven and driver pulleys, γ_1 and γ_2, with Coulomb friction and EPP friction are shown in Figures 42 - 43. The sliding angle indicate the direction of the friction force relative to the normal plane. For the driven pulley, the sliding angle is relatively constant during seating for most of the belt-pulley contact arc. However, for low tension spans, the sliding angle drastically decreases as the belt exits the pulley. The sharp changes in the sliding angles in the exit zones are caused by the sharp decrease in the belt radial displacement. Because the sharp changes in the sliding angle occur as the belt exits the pulley, the elasticity of the EPP friction model cannot smooth these sharp changes.

The minimum possible high tension while keeping the low tension at 200 N, was found for both friction models. The lowest value for T_H with Coulomb's Law was 562 N, while with the EPP friction model, the lowest value for T_H was 575 N. That is only about a 0.2% decrease in the solvable range for T_H with the EPP friction model. The EPP friction model was unable to smooth sharp changes in the inclination and sliding angles because the sharp changes occurred when the belt exits the pulley. In these cases, the belt is in the fully-slipping zone.

The results from the v-belt model with Coulomb's Law and the EPP friction model are shown in Tables 4 and 5, respectively. The tables show the constant values resulting from

the trivial equations, (117), (122), and (134), for each of the four high tension values. For high tensions of 1200 N and 3000 N, the results from the solutions with EPP friction model are very similar to the solutions with Coulomb's Law. However, the solutions for the wrap angles, Φ_1 and Φ_2, and the angular velocity of the driven pulley, ω_1, are not as similar when the high tensions are at their maximum possible value of 7781.2 N.

3.3 Summary

In this chapter, the Elastic/Perfectly-Plastic friction model was incorporated into the governing equations for a two-pulley v-belt system with equal pulley radii. It was used because the EPP friction law is a more physically-motivated model than previous regularized friction models, such as the creep-rate-dependent friction model. In this analysis, the belt tension, belt inclination angle, belt radial displacement, and the belt axial displacement were considered. The governing differential equations of these states were solved with a boundary value solver in MATLAB and compared to results with Coulomb's Law from previous studies.

It was found that the distributions of the belt states were very similar for the two friction models. However, the range of solvable tension differences was about 0.2% lower for the model with EPP friction. The sharp changes in the inclination and sliding angles at the exit points on both pulleys for very low and high tension spans contribute to the failure of both models. Because the sharp changes occur when the belt exits the pulley, the EPP friction law cannot reduce the corresponding sharp changes of these parameters and the sharp changes in the states cannot be smoothed.

CHAPTER IV

CONCLUSIONS

Belt drives are a ubiquitous element in numerous applications that transmit power between various machine elements. One limitation of the use of belt drives is the poor convergence of complex models that predict their operating conditions. This drawback greatly restricts the application of belt drive systems in some important manufacturing industries. A source of convergence failure is the sharp discontinuities in the solution due to the Coulomb friction model. It is believed that the inclusion of an elastic/perfectly-plastic friction law into the belt/pulley contact mechanics can yield mathematical models with enhanced accuracy and convergence. This thesis applied the physically-motivated Elastic/Perfectly-Plastic friction model to the problem of flat-belt and v-belt drives. The model more accurately captures the true behavior of an elastic belt that exhibits microslip prior to fully-developed slip than previous regularized friction models, such as the Creep-Rate-Dependent friction model.

In Chapter 2, the Elastic/Perfectly-Plastic friction model was introduced and applied to a two-pulley flat belt system. The equations of motions and the equilibrium solutions were derived using Hamilton's Principle. Solution to these equations is difficult because of the piece-wise linear nature of the governing partial differential equations. The stability of the perturbations to the steady-solutions was determined from an eigenvalue/eigenvector analysis, and it was found that the steady-state solution was stable. The results with the analytical solution developed in Chapter 2 matched very well with the results from a finite element model. It was found that if the EPP spring stiffness is too small, then the belt cannot undergo the prescribed tension change. If the value for the EPP spring stiffness is too large, then the EPP model approaches Coulomb's Law and sharp changes appear at the transition angle. Therefore, the EPP spring stiffness must be chosen appropriately such that the belt can still undergo the prescribed tension change, but also not too large that sharp changes in the normal and tension distributions appear at the transition point.

In Chapter 3, the Elastic/Perfectly-Plastic friction model was applied to a previously studied v-belt model. It was found that the solutions to the governing equations with the EPP friction model were similar to the solutions with the Coulomb friction model. The convergence properties of the v-belt model with EPP friction was very similar to that with Coulomb friction. When compared to the model with Coulomb friction, the range of possible high tensions for a given low tension was reduced slightly by 0.2% for the EPP friction. Convergence fails due to sharp changes of the inclination angle and the sliding angle. Because the sharp changes occur when the belt exits the pulley, the belt is in the fully-slipping zone and the EPP friction model cannot smooth the sharp changes in slope of the belt mechanics.

The results in this thesis provide an insight to improve convergence of complex belt models. The Elastic/Perfectly-Plastic friction model removed sharp changes in belt mechanics for flat belt systems. However, because the elastic portion of the EPP friction model occurs at the inlet of the belt-pulley contact zone, it could not smooth sharp changes in slope at the exit of the belt-pulley contact zone. Therefore, the v-belt model should incorporate more elasticity, or compliance, throughout the entire belt-pulley contact zone. This could be achieved by adding beam bending to the v-belt model.

APPENDIX A

MAPLE WORKSHEET TO FIND TRANSITION ANGLE, S^*_{DN}, AND INITIAL TENSION, T_{DN_O}, FOR THE DRIVEN PULLEY

```
> restart;
```

For EPP Section:
with boundary conditions: Te(0)=TL, ue(0)=0

```
> Te:= s-> To+EA*diff(ue(s),s):
> EqnE:= diff(Te(s),s)-m*vL^2*diff(ue(s),s,s)-kf*ue(s)=0:
> ue_sol:=dsolve({EqnE, eval(Te(s),s=0)=TL}, ue(s)):
  ue:=rhs(ue_sol):
> C2sol:=solve(subs(s=0,ue)=0,_C2):
  _C2:=C2sol:
> uepp:=simplify(ue):
```

For Coulomb Section:
with boundary conditions: Tc(R pi)=TH

```
> Tc:=s-> To+EA*diff(uc(s),s):
> EqnC:= diff(Tc(s),s)-m*vL^2*diff(uc(s),s,s)-muDN*Tc(s)/R=0:
> uc_sol:=dsolve({EqnC,eval(Tc(s),s=R*Pi)=TH}, uc(s)):
> uc:=rhs(uc_sol):
> ucol:=simplify(uc):
```

Use additional Boundary Conditions:
BC4: ue(s*) = ucs*):
BC5: Te(s*) = Tc(s*):
BC6: kf*ue(s*) = (mu/R)Tc(s*):

```
> duepp:=diff(uepp,s):
  ducol:=diff(ucol,s):
  Tepp:=To+EA*duepp:
  Tcol:=To+EA*ducol:
> BC4:=simplify(subs(s=sDN,uepp=ucol)):
> BC5:=simplify(subs(s=sDN,Tepp=Tcol)):
> BC6:=simplify(subs(s=sDN,kf*uepp=muDN/R*Tcol)):
```

Solve for s*, To and a constant of integration, C3:

```
> T_Sola:=solve({BC4,BC5,BC6}, {sDN,To,_C3}):
  assign(T_Sola):
```

APPENDIX B

MAPLE WORKSHEET TO FIND TRANSITION ANGLE, S^*_{DR}, AND INITIAL TENSION, T_{DR_O}, FOR THE DRIVER PULLEY

```
> restart;
```

For EPP Section:
with boundary conditions: Te(0)=TH, ue(0)=0

```
> Te:= s-> To+EA*diff(ue(s),s):
> EqnE:= diff(Te(s),s)-m*vL^2*diff(ue(s),s,s)-kf*ue(s)=0:
> ue_sol:=dsolve({EqnE, eval(Te(s),s=0)=TH}, ue(s)):
  ue:=rhs(ue_sol):
> C2sol:=solve(subs(s=0,ue)=0,_C2):
  _C2:=C2sol:
> uepp:=simplify(ue):
```

For Coulomb Section:
with boundary conditions: Tc(R pi)=TL

```
> Tc:=s-> To+EA*diff(uc(s),s):
> EqnC:= diff(Tc(s),s)-m*vL^2*diff(uc(s),s,s)-muDN*Tc(s)/R=0:
> uc_sol:=dsolve({EqnC,eval(Tc(s),s=R*Pi)=TL}, uc(s)):
> uc:=rhs(uc_sol):
> ucol:=simplify(uc):
```

Use additional Boundary Conditions:
BC4: ue(s*) = ucs*):
BC5: Te(s*) = Tc(s*):
BC6: kf*ue(s*) = (mu/R)Tc(s*):

```
> duepp:=diff(uepp,s):
  ducol:=diff(ucol,s):
  Tepp:=To+EA*duepp:
  Tcol:=To+EA*ducol:
> BC4:=simplify(subs(s=sDN,uepp=ucol)):
> BC5:=simplify(subs(s=sDN,Tepp=Tcol)):
> BC6:=simplify(subs(s=sDN,kf*uepp=muDN/R*Tcol)):
```

Solve for s*, To and a constant of integration, C3:

```
> T_Sola:=solve({BC4,BC5,BC6}, {sDN,To,_C3}):
  assign(T_Sola):
```

APPENDIX C

MAPLE WORKSHEET TO FIND THE MINIMUM EPP SPRING CONSTANT, K_F

```
> restart;
```

EPP Section only:
with BC's: Te(0)=TL, Te(R*Pi)=TH and ue(0)=0:

```
> Te:= s-> To+EA*diff(ue(s),s):
> EqnE:= diff(Te(s),s)-m*vL^2*diff(ue(s),s,s)-kf*ue(s)=0:
> ue_sol:=dsolve({EqnE, eval(Te(s),s=0)=TL,eval(Te(s),s=R*Pi)=TH},
  ue(s)):
  uepp:=simplify(rhs(ue_sol)):
> Tosol := solve(subs(s = 0, uepp) = 0, To):
  To := Tosol:
```

Use additional Boundary Conditions:
BC4: kf*ue(s*) = mu/R*Te(s*):
Assign numerical values for system parameters and find where bc4 crosses the x-axis:

```
> TL:=151.0: TH:=700.0: muDN:=1.2: EA:=80068.0: R:=0.08125: m:=
  0.1036: vL:=114.0*R:
> bc4:=simplify(subs(s=R*Pi,kf*uepp-muDN/R*(TH-m*vL^2))):
> plot(bc4,kf=1e3..1e8);
```

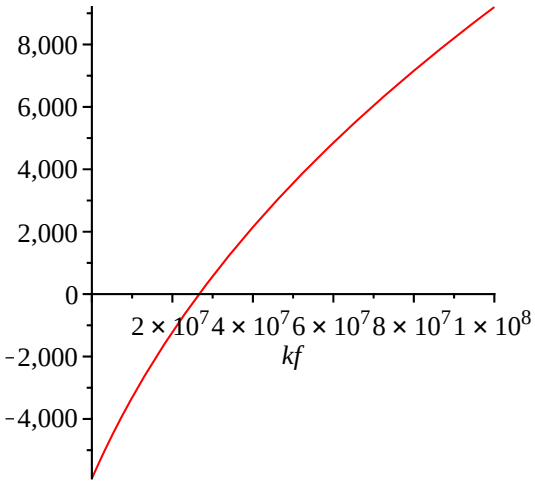


```
> BC4:=simplify(subs(s=R*Pi,kf*uepp-muDN/R*TH=0)):
> T_Sol:=fsolve({BC4}, {kf},2e7..4e7):
  assign(T_Sol);
>
>
```

APPENDIX D

MATLAB CODE FOR V-BELT SYSTEM WITH EPP FRICTION

```
function PulleySystem_EPPModel

global S_EA S_mu S_mo S_R S_beta S_k S_F_slack S_F_tight S_W_DR S_PulleyDistance
global y1 y2 y3 y4 y5 y6 y7 y8 y9 y10 y11 y12 y13 y14 y15 y16 y17
global kf_DN kf_DR
kf_DN=81e5;
kf_DR=81e5;
S_EA=120000;        S_mu=0.4;           S_mo=0.108;
R=0.25;           beta=18*pi/180;   S_k=900000;
F_slack=100;      F_tight=576;     S_W_DR=1000*2*pi/60;
S_PulleyDistance=1.393327732346075e+000;

%To get the initial guess. Important step!
[XX,y1,y2,y3,y4,y5,y6,y7,y8,y9,y10,y11,y12,y13,y14,y15]=InitialGuess_EPPsystem;

%warning off MATLAB:bvp4c:RelTolNotMet;
options = bvpset('stats','on','RelTol',1e-3);
solinit = bvpinit(linspace(0.0, 1.0 ,51),@ex3init_tight);
sol = bvp4c(@TightSpan2ode,@TightSpan2bc,solinit, options);

options = bvpset('stats','on','RelTol',1e-3);
sol = bvp4c(@TightSpan2ode,@TightSpan2bc,solinit, options);

% %-------------------------------------------------------------------
% %Continuation method for increasing F_tight......
% for k=1:1:10
%     k
%     F_tight=F_tight*1.1
%     options = bvpset(options,'RelTol',1e-3);
%     sol = bvp4c(@TightSpan2ode,@TightSpan2bc,sol,options);
% end
% %-------------------------------------------------------------------
% %Continuation method for decreaseing F_tight......
% for k=1:1:20
%     k
%     F_tight=F_tight/1.0001
%     kf_DN=kf_DN/1.1
%     kf_DR=kf_DR/1.1
%     options = bvpset(options,'RelTol',1e-3);
%     sol = bvp4c(@TightSpan2ode,@TightSpan2bc,sol,options);
% end
% for k=1:1:489
%     k
%     F_tight=F_tight/1.0001
%     options = bvpset(options,'RelTol',1e-3);
%     sol = bvp4c(@TightSpan2ode,@TightSpan2bc,sol,options);
% end
% %-------------------------------------------------------------------
```

```
t = sol.x;  y = sol.y;

F_DN=y(1,:);    thita_DN=y(2,:);    x_DN=y(3,:);    W_DN=y(4,1);
F_DR=y(1+7,:);  thita_DR=y(2+7,:);  x_DR=y(3+7,:);  G=y(4+7,1);
T_DN=F_2_T(F_DN, S_EA, G, S_mo);
T_DR=F_2_T(F_DR, S_EA, G, S_mo);
omega_DN=zeros(length(thita_DN),1);
omega_DN(1,1)=W_DN;
G_DR=zeros(length(thita_DN),1);
G_DR(1,1)=G;

wrap_DN=y(7,1);
wrap_DR=y(7+7,1);

phi_DN=zeros(length(thita_DN),1);
phi_DN(1,1)=wrap_DN;
phi_DR=zeros(length(thita_DR),1);
phi_DR(1,1)=wrap_DR;

Length_slackspan=y(15,1);
uhat_DN=y(16,:);
uhat_DR=y(17,:);

[gama_DR]=GetGama(thita_DR, x_DR, T_DR, S_mo, S_W_DR, G, R, S_EA, 0);
[gama_DN]=GetGama(thita_DN, x_DN, T_DN, S_mo, W_DN, G, R, S_EA, 1);

tan_beta_s_DN=tan(beta)*cos(gama_DN);
cos_beta_s_DN=1./sqrt(1+(tan_beta_s_DN).^2);
sin_beta_s_DN=tan_beta_s_DN.*cos_beta_s_DN;
pc_DN=S_k*x_DN/2./(cos(beta)+mu*sin_beta_s_DN);
pe_DN=(S_k*x_DN/2-kf_DN*uhat_DN.*sin_beta_s_DN)/cos(beta);

for i=1:length(x_DN)
    if abs(uhat_DN(i)) < abs(mu*pc_DN(i)/kf_DN)
        f_DN(i)=kf_DN*uhat_DN(i);
        p_DN(i)=pe_DN(i);
        fflag_DN(i)=0;
    else
        f_DN(i)=mu*pc_DN(i);
        p_DN(i)=pc_DN(i);
        fflag_DN(i)=1;
    end
end

tan_beta_s_DR=tan(beta)*cos(gama_DR);
cos_beta_s_DR=1./sqrt(1+(tan_beta_s_DR).^2);
sin_beta_s_DR=tan_beta_s_DR.*cos_beta_s_DR;
pc_DR=S_k*x_DR/2./(cos(beta)+mu*sin_beta_s_DR);
pe_DR=(S_k*x_DR/2-kf_DR*uhat_DR.*sin_beta_s_DR)/cos(beta);
```

```
for i=1:length(x_DR)
    if abs(kf_DR*uhat_DR(i)) < abs(mu*pc_DR(i))
        f_DR(i)=kf_DR*uhat_DR(i);
        p_DR(i)=pe_DR(i);
        fflag_DR(i)=0;
    else
        f_DR(i)=mu*pc_DR(i);
        p_DR(i)=pc_DR(i);
        fflag_DR(i)=1;
    end
end

figure; plot((180/pi)*t*wrap_DR, F_DR); title('System: Tension DR [N]');
figure; plot((180/pi)*t*wrap_DR, (180/pi)*thita_DR); hold on;
plot((180/pi)*t*wrap_DR, 0*thita_DR, 'r'); title('System: theta DR [deg]');
figure; plot((180/pi)*t*wrap_DR, x_DR); title('System: x DR [m]');
figure; plot((180/pi)*t*wrap_DR, gama_DR*180/pi); title('System: gamma DR [deg]');
figure; plot((180/pi)*t*wrap_DR, y(6+7,:)); title('System: stress-free length DR [m]');
figure; plot((180/pi)*t*wrap_DR, uhat_DR); title('uhat DR [m]');
figure; plot((180/pi)*t*wrap_DN, F_DN); title('System: Tension DN [N]');
figure; plot((180/pi)*t*wrap_DN, (180/pi)*thita_DN); hold on;
plot((180/pi)*t*wrap_DN, 0*thita_DN, 'r'); title('System: theta DN [deg]');
figure; plot((180/pi)*t*wrap_DN, x_DN); title('System: x DN [m]');
figure; plot((180/pi)*t*wrap_DN, gama_DN*180/pi); title('System: gamma DN [deg]');
figure; plot((180/pi)*t*wrap_DN, y(6,:)); title('System: stress-free length DN [m]');
figure; plot((180/pi)*t*wrap_DR, y(15,:)); title('System: slack span length [m]');
figure; plot((180/pi)*t*wrap_DN, uhat_DN); title('uhat DN [m]');

%Plot system steady state
phai_DR=t*wrap_DR;     phai_DN=t*wrap_DN;
[Length]=Plot_System(thita_DR,x_DR,phai_DR,wrap_DR,thita_DN,x_DN,phai_DN,wrap_DN,...
        Length_slackspan,R,S_PulleyDistance);

%=========================================================================
function dydt = TightSpan2ode(t,y)
global S_EA mu S_mo R beta S_k F_slack F_tight
global S_W_DR kf_DN kf_DR

F_DN=y(1);      thita_DN=y(2);      x_DN=y(3);      W_Driven=y(4);
F_DR=y(1+7);    thita_DR=y(2+7);    x_DR=y(3+7);    G=y(4+7);
uhat_DN=y(16);
uhat_DR=y(17);

wrap_DN=y(7);
wrap_DR=y(7+7);

%--------driven pulley------------------------------
T_DN=F_2_T(F_DN, S_EA, G, S_mo);

Numerator_DN=cos(thita_DN)-(S_mo*W_Driven/G)*(R-x_DN)/(1+T_DN/S_EA);
Denominator_DN=sin(thita_DN);
```

```
cos_gama_DN=Denominator_DN/sqrt(Numerator_DN^2+Denominator_DN^2);
sin_gama_DN=Numerator_DN/sqrt(Numerator_DN^2+Denominator_DN^2);

tan_beta_s_DN=tan(beta)*cos_gama_DN;
cos_beta_s_DN=1/sqrt(1+(tan_beta_s_DN)^2);
sin_beta_s_DN=tan_beta_s_DN*cos_beta_s_DN;

pc_DN=S_k*x_DN/(2*(cos(beta)+mu*sin_beta_s_DN));
pe_DN=(S_k*x_DN/2-kf_DN*uhat_DN*sin_beta_s_DN)/cos(beta);

if abs(uhat_DN) < abs(mu*pc_DN/kf_DN)
    f_DN=kf_DN*uhat_DN;
    p_DN=pe_DN;
else
    f_DN=mu*pc_DN;
    p_DN=pc_DN;
end
%--------driver pulley-----------------------------
T_DR=F_2_T(F_DR, S_EA, G, S_mo);

Numerator_DR=cos(thita_DR)-(S_mo*S_W_DR/G)*(R-x_DR)/(1+T_DR/S_EA);
Denominator_DR=sin(thita_DR);
cos_gama_DR=Denominator_DR/sqrt(Numerator_DR^2+Denominator_DR^2);
sin_gama_DR=Numerator_DR/sqrt(Numerator_DR^2+Denominator_DR^2);

tan_beta_s_DR=tan(beta)*cos_gama_DR;
cos_beta_s_DR=1/sqrt(1+(tan_beta_s_DR)^2);
sin_beta_s_DR=tan_beta_s_DR*cos_beta_s_DR;

pc_DR=S_k*x_DR/(2*(cos(beta)+mu*sin_beta_s_DR));
pe_DR=(S_k*x_DR/2-kf_DR*uhat_DR*sin_beta_s_DR)/cos(beta);

if abs(kf_DR*uhat_DR) < abs(mu*pc_DR)
    f_DR=kf_DR*uhat_DR;
    pDR=peDR;
else
    fDR=mu*pcDR;
    pDR=pcDR;
end
%-----------------------------------------------------
dydt = [
    wrapDN*2*(-pDN*sin(beta)*tan(thDN)+fDN*cbetasDN*(tan(thDN)*cgamDN+sgamDN))*(R-xDN)
    wrapDN*(1-(2/FDN)*(pDN*sin(beta)-fDN*cbetasDN*(cgamDN-sgamDN*sin(thDN)/cos(thDN)))*(R-xDN))
    wrapDN*((-1)*(R-xDN)*tan(thDN))
    0               % Unknown rotational driven pulley speed
    wrapDN*2*fDN*cbetasDN*sgamDN*(R-xDN)^2/cos(thDN)
    wrapDN*(R-xDN)/(cos(thDN)*(1+TDN/S_EA))    %For stress-free length
    0               %Unknown wrap for driven pulley ====================================
    wrapDR*2*(-pDR*sin(beta)*tan(thDR)+fDR*cbetasDR*(tan(thDR)*cgamDR+sgamDR))*(R-xDR)
    wrapDR*(1-(2/FDR)*(pDR*sin(beta)-fDR*cbetasDR*(cgamDR-sgamDR*sin(thDR)/cos(thDR)))*(R-xDR))
    wrapDR*((-1)*(R-xDR)*tan(thDR))
```

```
    0               % Unknown mass flow rate G
    wrapDR*2*fDR*cbetasDR*sgamDR*(R-xDR)^2/cos(thDR)
    wrapDR*(R-xDR)/(cos(thDR)*(1+TDR/S_EA))    %For stress-free length
    0               %Unknown wrap for driver pulley
    0               %Unknown slack span length.
    wrapDN*(TDN-F_slack)/S_EA*(R-xDN)/cos(thDN)    % uhat for DN pulley
    wrapDR*(TDR-F_tight)/S_EA*(R-xDR)/cos(thDR)];  % uhat for DR pulley

function res = TightSpan2bc(ya,yb)
global F_slack F_tight R S_PulleyDistance
DN0=ya(2);      DN1=yb(2);
DR0=ya(2+7);    DR1=yb(2+7);
WrapDN=ya(7);   WrapDR=ya(7+7);
InclineAngleDR=-(pi-DR1)-WrapDR-DR0;
InclineAngleDN=WrapDN+DN0-DN1;

L_slackspan=ya(15);
MidAngle_SW=pi/2-DR1;
MidAngle_NW=3*pi/2-WrapDR+DR1;
MidAngle_SE=pi/2+DN0;
MidAngle_NE=3*pi/2-WrapDN-DN0;

x_C1=-L_slackspan/2-R*(cos(MidAngle_SW)-cos(MidAngle_NW));
y_C1=R*(sin(MidAngle_SW)+sin(MidAngle_NW));
x_C2=L_slackspan/2+R*(cos(MidAngle_SE)-cos(MidAngle_NE));
y_C2=R*(sin(MidAngle_SE)+sin(MidAngle_NE));

x_01=-L_slackspan/2-R*cos(MidAngle_SW);
y_01=R*sin(MidAngle_SW);
x_02=L_slackspan/2+R*cos(MidAngle_SE);
y_02=R*sin(MidAngle_SE);

res = [ ya(1)-F_slack                              % F(0)=F_slack
        ya(3)                                      % x(0)=0
        yb(1)-F_tight                              % F_2(0)=F_tight
        yb(3)
        ya(5)                                      % for torque
        ya(6)                                      % for stress-free length
        ya(1+7)-F_tight                            % F(0)=F_slack
        ya(3+7)                                    % x(0)=0
        yb(1+7)-F_slack                            % F_2(0)=F_tight
        yb(3+7)
        ya(5+7)                                    % for torque
        ya(6+7)                                    % for stress-free length
        tan(InclineAngleDR)-tan(InclineAngleDN)
        (y_C1-x_C1*tan(InclineAngleDR))-(y_C2-x_C2*tan(InclineAngleDN))
        (x_01-x_02)^2+(y_01-y_02)^2-S_PulleyDistance^2
        ya(16)
        ya(17)];
```

```
function Vv = ex3init_tight(x)
global  y1 y2 y3 y4 y5 y6 y7 y8 y9 y10 y11 y12 y13 y14 y15
n=0;
for kk=0:1/(51-1):1
    n=n+1;
    if (abs(x-kk)<0.00001)
        II=n;
    end
end

Vv = [  y1(II)
        y2(II)
        y3(II)
        y4(II)
        y5(II)
        y6(II)
        y7(II)
        y8(II)
        y9(II)
        y10(II)
        y11(II)
        y12(II)
        y13(II)
        y14(II)
        y15(II)
        x^2
        -x];
```

REFERENCES

[1] Bechtel, S., Vohra, S., Jacob, K., and Carlson, C., "The stretching and slipping of belts and fibers on pulleys," *Journal of Applied Mechanics*, vol. 67, pp. 197–206, 2000.

[2] Beikmann, R., Perkins, N., and Ulsoy, A., "Nonlinear coupled vibration response of serpentine belt drive systems," *Journal of Vibration and Acoustics*, vol. 118, pp. 567–574, 1996.

[3] Fawcett, J., "Chain and belt drives - a review," *Shock and Vibration Digest*, vol. 13, no. 5, pp. 5–12, 1981.

[4] Ferri, A., "Friction damping and isolation systems," *Journal of Vibration and Acoustics*, vol. 117, pp. 196–205, 1995.

[5] Firbank, T., "Mechanics of the belt drive," *International Journal of Mechanical Science*, vol. 12, pp. 1053–1063, 1970.

[6] Gerbert, G. and Sorge, F., "Full sliding adhesive-like contact of v-belts," *Journal of Mechanical Design*, vol. 124, pp. 706–712, 2002.

[7] Hwang, S. and Perkins, N., "Supercritical stability of an axially moving beam: Parts i and ii," *Journal of Sound and Vibration*, vol. 154, no. 3, pp. 381–409, 1992.

[8] Johnson, K., *Contact Mechanics*. New York, NY: Cambridge University Press, 1985.

[9] Kong, L. and Parker, R. G., "Microslip friction in flat belt drives," *Journal of Mechanical Engineering Science*, vol. 219, pp. 1097–1106, 2005.

[10] Kong, L. and Parker, R. G., "Steady mechanics of belt-pulley systems," *Journal of Applied Mechanics*, vol. 72, pp. 25–34, 2005.

[11] Kong, L. and Parker, R. G., "Vibration of an axially moving beam wrapping on fixed pulleys," *Journal of Sound and Vibration*, vol. 280, pp. 1066–1074, 2005.

[12] Kong, L. and Parker, R. G., "Mechanics and sliding friction in belt drives with pulley grooves," *Journal of Mechanical Design*, vol. 128, pp. 494–502, 2006.

[13] Leamy, M. J., "On a perturbation method for the analysis of unsteady belt-drive operation," *Transactions of the ASME*, vol. 72, pp. 570–580, 2005.

[14] Leamy, M. J. and Wasfy, T. M., "Analysis of belt-drive mechanics using a creep-rate-dependent friction law," *Journal of Applied Mechanics*, vol. 69, pp. 763–771, 2002.

[15] Leamy, M. J. and Wasfy, T. M., "Transient and steady-state dynamic finite element modeling of belt-drives," *Journal of Dynamics Systems, Measurement, and Control*, vol. 124, pp. 575–581, 2002.

[16] Lee, U. and Jang, I., "On the boundary conditions for axially moving beams," *Journal of Sound and Vibration*, vol. 306, pp. 675–690, 2007.

[17] Makris, N. and Constantinou, M., "Analysis of motion resisted by friction. ii. velocity-dependent friction," *Mechanics Based Design of Structures and Machines*, vol. 19, no. 4, pp. 501–526, 1991.

[18] Meirovitch, L., "A new method of solution of the eigenvalue problem for gyroscopic systems," *AIAA Journal*, vol. 12, pp. 1337–1342, 1974.

[19] Meirovitch, L., "A modal analysis for the response of linear gyroscopic systems," *Journal of Applied Mechanics*, vol. 42, no. 2, pp. 446–450, 1975.

[20] Menq, C., Bielak, J., and Griffin, J., "The influence of microslip on vibratory response, part i: A new microslip model," *Journal of Sound and Vibration*, vol. 107, no. 2, pp. 279–293, 1986.

[21] Oden, J. and Martins, J., "Models and computational methods for dynamic friction phenomena," *Computer Methods in Applied Mechanics and Engineering*, vol. 52, pp. 527–634, 1985.

[22] Pellicano, F. and Vestroni, F., "Non-linear dynamics and bifurcations of an axially moving beam," *Journal of Vibration and Acoustics*, vol. 122, pp. 21–30, 2001.

[23] Rubin, M., "An exact solution for steady motion of an extensible belt in multipulley belt drive systems," *Journal of Mechanical Design*, vol. 122, pp. 311–316, 2000.

[24] Shampine, L. F., Kierzenka, J., and Reichelt, M. W., "Solving boundary value problems for ordinary differential equations in matlab with bvp4c," 2000.

[25] http://david-ho.com/engr102/images/cvt01.jpg.

[26] http://img.alibaba.com/photo/10272819/High_Power_V_belt.jpg.

[27] https://www.centralvacuumstores.com/images/lg/cvs/eureka_flat_belt.jpg.

[28] http://www.four-h.purdue.edu/tractor/pictures/028.jpg.

[29] Wickert, J., "Non-linear vibration of a traveling tensioned beam," *International Journal of Non-Linear Mechanics*, vol. 27, no. 3, pp. 503–517, 1992.

[30] Wickert, J. and Mote, C., "Current research on the vibration and stability of axially moving materials," *Shock and Vibration Digest*, vol. 20, pp. 3–13, 1988.

[31] Wickert, J. and Mote, C., "Classical vibration analysis of axially moving continua," *Journal of Applied Mechanics*, vol. 57, no. 3, pp. 738–744, 1990.